Sensors & Actuators: B. Chemical 360 (2022) 131682

Contents lists available at ScienceDirect

Sensors and Actuators: B. Chemical

journal homepage: www.elsevier.com/locate/snb

Mass identification of multiple particles on a doubly clamped resonator

Chenxi Wei [a,b], Yin Zhang [a,b,*]

[a] State Key Laboratory of Nonlinear Mechanics (LNM), Institute of Mechanics, Chinese Academy of Sciences, Beijing 100190, China
[b] School of Engineering Science, University of Chinese Academy of Sciences, Beijing 100049, China

ARTICLE INFO

Keywords:
Mass resonator sensor
Multi-particle identification
Mass sensing
Inverse problem
Timoshenko beam model

ABSTRACT

The shift of resonant frequencies is the working mechanism of a mass resonator sensor. The shift is due to the adsorption of particles, which can change the mass, stiffness and damping of the sensor. Based on the Timoshenko beam model, an analytical model and mathematical solution are proposed to explain the frequency shifts due to the adsorption of multiple particles. The model shows a better accuracy in the scenarios of the high order resonance, the vibration in the viscous environment and under high tension. The inverse problem of identifying multi-particle mass is solved by an iteration algorithm, whose performance is also evaluated for the measured noise and adsorption areas. The mass identification of multiple particles shows a better sensitivity and robustness than that of single particle, which is somewhat surprising but beneficial to mass sensing. The results in this study provide a theoretical basis for the mass identification of multiple particles and are of some help to the practical application.

1. Introduction

The application of micro/nano-structures as mass resonators has attracted increasing attention because of their numerous use prospects in molecular detection, such as the detection of drug [1], deoxyribonucleic acid (DNA) [2], virus [3] and gas [4]. Nowadays, based on the dynamic modes to identify attached mass, the sensitivity, swiftness, effectiveness and robustness of a mass resonator are urgent to be improved [5–8].

When a molecule is adsorbed on a nano-mechanical mass resonator, its added mass effect reduces the resonant frequencies of the resonator, which is a high-throughput identification [9]. The measurement efficiency and sensitivity are higher as the dimension of a mass sensor scales down. Therefore, fabricating the micro-scaled or even nano-scaled mass resonator is still an effective approach to achieve a high performance with ultrahigh sensitivity [10]. Furthermore, in order to improve the sensitivity of the device, other effective approaches are the high-order resonance and the high quality factor (Q-factor) [11]. The high-order resonance allows the mass sensors to measure particle masses with a greater sensitivity [12–14], which indicates that the sensitivity increases with mode number. The Q-factor is directly determined by the damping, which is usually related to the dimension, material and environment of mass resonators [15–18]. Using high tensile-stress technology on mass resonators can significantly increase the Q-factor and sensitivity, which makes a beam behave like a string [19,20]. Because a buckled structure can enlarge frequency shifts as a result of the gas attachment increase [21], the wrinkle structure created by the hydrothermal method enhances the gas analyte response [22]. The suspended microfluidic channels formed by the sacrificial silicon dioxide process are with a high Q-factor, in vacuum, which is suitable for the detection of biological samples, such as cells [23].

Measuring a particle mass is complicated by the issue of determining its position, which makes mass sensing extremely challenging [23]. There are some straightforward methods to determine the particle position, for example, trapping the particles in certain position by filtering them [24]. But the particles in detection are required to be in particular size. Via the least-squares criterion, it is possible to solve the inverse problem numerically [25]. Through the relationship between the frequency shifts and particle mass, position, the calculated mass of one gold bead is in agreement with the actual one [26]. Based on the analytical analysis that has been conducted on the axial vibration of a rod, it shows that the position of one mass can be determined from the frequency shifts of two modes [27], which has been applied on mass sensors [28]. The mass spectrometry based on the nano-electromechanical systems (NEMS) is employed in real time for the mass and position determination of one single protein, which is sensitive on the mass increase [29]. Furthermore, the inertial imaging method is developed on measuring the mass, molecular size and shape of one particle [30]. By using the

* Corresponding author at: State Key Laboratory of Nonlinear Mechanics (LNM), Institute of Mechanics, Chinese Academy of Sciences, Beijing 100190, China.
E-mail address: zhangyin@lnm.imech.ac.cn (Y. Zhang).

https://doi.org/10.1016/j.snb.2022.131682
Received 27 August 2021; Received in revised form 22 January 2022; Accepted 7 March 2022
Available online 9 March 2022

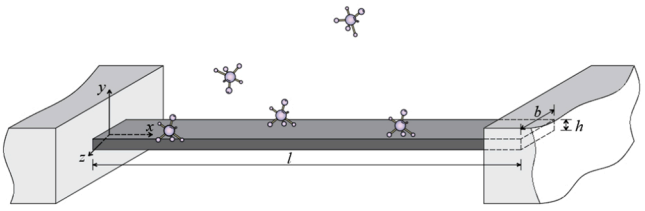

Fig. 1. Schematic of doubly clamped beam with particles adsorbed on surface.

approximate analytical solution of resonant frequencies, the mass and position of one particle can be decoupled and determined by the three frequencies at most [31]. Moreover, the inverse problem of mass identification together with particle position and axial stress is solved, in which the axial stress can improve the mass sensing [32]. And the inverse problem of a string resonator, the determination of mass, position and surface force induced by one particle, is studied [33]. By using the strain gradient theory to simulate nanoscale effect on the nanorod with concentrated mass, the closed-form expression for the mass is obtained based on the data of frequency shifts [34]. The application of the arrays of nano-mechanical resonators promotes the effectiveness and resolution to reach a reliable result [35].

Compared with the above studies of one particle case, the mass identification of multi-particles is much more difficult than that of single particle. The mass and position of every particle can affect the frequencies of the resonator [36]. In the inversion process, the numerical instability occurs more easily with more variables. To run the inversion program for mass identification, for a case of the Nelder–Mead simplex algorithm [37], the initial guess is vital for the inversion computation. The reason is that the nonlinear relationship between the particle position and the resonant frequency [26] leads to great difficulties, especially for the gradient based algorithms. The focus on the mass identification of multi-particles is to overcome the difficulty brought by this nonlinear relationship. The closed form solution of the two cracks estimation on a simply supported beam [38] provides a theoretical basis for the mass identification of two particles. The scanning method [39] offers an alternative approach for multiple particles or cracks detection. However, to attain a high throughput detection asks for the evaluation of massive samples in a short time [40]. Therefore, for a wider application of the mass sensors such as artificial nose [41,42], the research on the multi-particles mass identification is a necessary step.

In this study, the analytical solution of the doubly clamped beam with multiple particles attached on surface is obtained. The Timoshenko beam model, axial stress and damping effect are used to describe the beam higher-order vibration. With the benefit of an integral transformation to reduce the oscillation relationship between frequencies and particle position, the mass identification process of solving the inverse problem is improved. In comparison with the results of three dimensional finite element method (3D-FEM) and experimental results, the method of the present model is validated, whose sensitivity variation with axial stress and damping is also investigated. The results obtained by solving the inverse problem are also validated by comparing with those of 3D-FEM. Furthermore, the analysis on the impact of the noise effect of frequencies and the initial positions of inversion process is presented, which can be very helpful to the design of mass resonator sensors.

2. Frequency shift from attached mass from mechanical model

Fig. 1 is a schematic diagram of a doubly clamped beam with several particles adsorbed on its surface. The beam length, width and thickness are denoted as l, b and h, respectively. In this study, the particles are assumed to be within same mass and sparsely distributed. In the mass identification of analytes in a real time analysis [29,43], the multiple particles are adsorbed on mass sensors, which improves the throughput of the electrospray injection (ESI) system. Furthermore, the total number of the attached particles is (assumed) known, which can be easily obtained by using the scanning electron microscope (SEM) technology [37].

Based on the Timoshenko beam model [44], the governing equations of the beam with particles attached on its surface, are as follows:

$$\begin{cases} EI\dfrac{\partial^2\psi}{\partial x^2}+\kappa GA\left(\dfrac{\partial w}{\partial x}-\psi\right)=\rho I\dfrac{\partial^2\psi}{\partial t^2}, \\ \kappa GA\left(\dfrac{\partial^2 w}{\partial x^2}-\dfrac{\partial\psi}{\partial x}\right)+T\dfrac{\partial^2 w}{\partial x^2}-D\dfrac{\partial w}{\partial t}=\left[\rho A+M\sum\limits_{i=1}^{nm}\delta(x-x_i)\right]\dfrac{\partial^2 w}{\partial t^2}, \end{cases} \tag{1}$$

where w, ψ and t are the transverse displacement of beam neutral surface, the rotation angle of cross section and time, respectively. E, G and ρ are Young's modulus, shearing modulus and density of the beam, respectively. Here, $I{=}bh^3/12$ is the moment of inertia; $A{=}bh$ is the cross-section area; $\kappa{=}10(1+\nu)/(12+11\nu)$ is the shear factor for rectangular cross-section [45] and ν is the Poisson's ratio. The Dirac function δ here is to model a particle as a concentrated mass; M, x_i and nm are mass, position and number of these particles respectively. D is the viscous damping coefficient [46] and T is the axial load. The positive T is tension and negative T is compression.

The clamped boundary conditions are the following:

$$w(0)=0,\ \ \psi(0)=0,\ \ w(l)=0,\ \ \psi(l)=0. \tag{2}$$

In this model, the parameters of E, I, G, A, T, D, ρ and κ are assumed unchanged before and after the adsorption of particles, for the attached mass is very small compared with the beam. The axial load T is due to the fabrication process of the beam and the adsorption is assumed to have no impact on T. The tensile axial load is beneficial for the sensitivity of mass sensors [19].

By introducing the quantities of $\xi=x/l$, $\tau=t\sqrt{\kappa G/\rho l^2}$, $W(\xi,\tau)=w/l$, $\Psi(\xi,\tau)=\psi$, Eq. (1) is now non-dimensionalized as follows:

$$\begin{cases} e\dfrac{\partial^2\Psi}{\partial\xi^2}+\dfrac{\partial W}{\partial\xi}-\Psi=r\dfrac{\partial^2\Psi}{\partial\tau^2}, \\ (1+s)\dfrac{\partial^2 W}{\partial\xi^2}-\dfrac{\partial\Psi}{\partial\xi}-d\dfrac{\partial W}{\partial\tau}=\left[1+m\sum\limits_{i=1}^{nm}\delta(\xi-\xi_i)\right]\dfrac{\partial^2 W}{\partial\tau^2}, \end{cases} \tag{3}$$

where ξ_i denotes the dimensionless location of a particle; The dimensionless quantities are defined as

$$e=\frac{EI}{\kappa GAl^2},\ \ d=\frac{Dl}{A\sqrt{\kappa G\rho}},\ \ r=\frac{I}{Al^2},\ \ s=\frac{T}{\kappa GA},\ \ m=\frac{M}{\rho Al}. \tag{4}$$

In this model, $e=Er_g^2/\kappa GA$ and $r{=}r_g^2$, where $r_g{=}\sqrt{3}h/(6\,l)$ is the dimensionless radius of gyration. In a beam structure, r_g is much less than 1, causing $e{\ll}\,1$ and $r\ll 1$.

Correspondingly, the dimensionless boundary conditions are the

following:

$$W(0)=0,\ \ \Psi(0)=0,\ \ W(1)=0,\ \ \Psi(1)=0. \tag{5}$$

The solution forms of W and Ψ are assumed as follows:

$$W(\xi,\tau)=\phi(\xi)e^{\lambda\tau},\quad \Psi(\xi,\tau)=\varphi(\xi)e^{\lambda\tau}, \tag{6}$$

By substituting Eq. (6) into Eqs. (3) and (5), and eliminating $\varphi(\xi)$, the following governing equation and boundary conditions are obtained as:

$$\begin{cases} e(1+s)\dfrac{\mathrm{d}^4\phi}{\mathrm{d}\xi^4}-\left[s-e\gamma d-e\left(\omega^2-\gamma^2\right)-(1+s)r\left(\omega^2-\gamma^2\right)\right]\dfrac{\mathrm{d}^2\phi}{\mathrm{d}\xi^2} \\ \qquad -\left[\gamma d+\left(\omega^2-\gamma^2\right)\right]\phi-m\sum\limits_{i=1}^{nm}\delta(\xi-\xi_i)\left(\omega^2-\gamma^2\right)\left(\phi-e\dfrac{\mathrm{d}^2\phi}{\mathrm{d}\xi^2}\right)=0, \\ [ed-2e\gamma-2(1+s)r\gamma]\dfrac{\mathrm{d}^2\phi}{\mathrm{d}\xi^2}-(d-2\gamma)\phi+2\gamma m\sum\limits_{i=1}^{nm}\delta(\xi-\xi_i)\left(\phi-e\dfrac{\mathrm{d}^2\phi}{\mathrm{d}\xi^2}\right)=0. \end{cases} \tag{11}$$

Here $\phi(\xi)$ is assumed with the following form:

$$e(1+s)\frac{\mathrm{d}^4\phi}{\mathrm{d}\xi^4}-\left[s+ed\lambda+e\lambda^2+(1+s)r\lambda^2\right]\frac{\mathrm{d}^2\phi}{\mathrm{d}\xi^2}+\left(1+r\lambda^2\right)\left(d\lambda+\lambda^2\right)\phi=m\sum_{i=1}^{nm}\delta(\xi-\xi_i)\left[e\lambda^2\frac{\mathrm{d}^2\phi}{\mathrm{d}\xi^2}-\lambda^2\left(1+r\lambda^2\right)\phi\right], \tag{7}$$

and

$$\begin{aligned} &\phi(0)=\phi(1)=0, \\ &e(1+s)\frac{\mathrm{d}^3\phi(0)}{\mathrm{d}\xi^3}+\left\{1-ed\lambda-e\lambda^2\left[1+m\sum_{i=1}^{nm}\delta(\xi-\xi_i)\right]\right\}\frac{\mathrm{d}\phi(0)}{\mathrm{d}\xi}=0, \\ &e(1+s)\frac{\mathrm{d}^3\phi(1)}{\mathrm{d}\xi^3}+\left\{1-ed\lambda-e\lambda^2\left[1+m\sum_{i=1}^{nm}\delta(\xi-\xi_i)\right]\right\}\frac{\mathrm{d}\phi(1)}{\mathrm{d}\xi}=0. \end{aligned} \tag{8}$$

In order to obtain the analytical solution of Eq. (7) with the given boundary conditions, two approximations should be used to simplify this problem: (1) Neglecting the terms associated with λ^3 and λ^4, which are small compared with lower order terms of λ, especially when the coefficient $r\ll 1$ in a beam structure [47]; (2) Neglecting the terms in boundary conditions whose coefficients contain e when $e\ll 1$. The governing equation and boundary condition are now approximated as follows:

$$\phi(\xi)=\sum_{j=j_0}^{j_0+ns-1}a_j\widehat{\phi}_j(\xi), \tag{12}$$

where j_0 is the starting mode number, ns is the total number of mode shapes, a_j is the constant to be determined and $\widehat{\phi}_j(\xi)$ is the mode shape of a doubly clamped beam under an axial tension with the following expression

$$\widehat{\phi}_j(\xi)=C_j^1\sin\left(g_j^1\xi\right)+C_j^2\cos\left(g_j^1\xi\right)+C_j^3\exp\left(-g_j^2\xi\right)+C_j^4\exp\left(g_j^2\xi\right), \tag{13}$$

where the coefficients are calculated from Appendix. A and the subscript j denotes the j-th eigenvalues.

By employing the Galerkin method on Eq. (11), the two sets of equations are obtained as follows:

$$e(1+s)\frac{\mathrm{d}^4\phi}{\mathrm{d}\xi^4}-\left[s+ed\lambda+e\lambda^2+(1+s)r\lambda^2\right]\frac{\mathrm{d}^2\phi}{\mathrm{d}\xi^2}+\left(d\lambda+\lambda^2\right)\phi=m\sum_{i=1}^{nm}\delta(\xi-\xi_i)\lambda^2\left(e\frac{\mathrm{d}^2\phi}{\mathrm{d}\xi^2}-\phi\right), \tag{9}$$

and

$$\phi(0)=\phi(1)=0,\ \ \frac{\mathrm{d}\phi(0)}{\mathrm{d}\xi}=\frac{\mathrm{d}\phi(1)}{\mathrm{d}\xi}=0. \tag{10}$$

The complex eigenvalue λ is assumed as $\lambda=-\gamma+i\omega$, where γ is the decay rate, ω is the resonant frequency and $i^2=-1$. By substituting this into Eq. (9) and then separating the Eq. (9) into the real and imaginary parts, the following governing equations are obtained:

$$\begin{cases} \mathbf{X}(\omega,\gamma)\cdot\mathbf{A}=\mathbf{0} \\ \mathbf{Y}(\gamma)\cdot\mathbf{A}=\mathbf{0} \end{cases}. \tag{14}$$

where the vector $\mathbf{A}=[a_{j_0},a_{j_0+1},a_{j_0+2},\ldots,a_{j_0+ns-1}]^{\mathrm{T}}$. By using the orthogonality of the mode shape $\widehat{\phi}_j(\xi)$, The elements of the matrix $\mathbf{X}=(X_{i,j})_{ns\times ns}$ and matrix $\mathbf{Y}=(Y_{i,j})_{ns\times ns}$ are expressed as follows:

$$\begin{aligned} X_{i,j}&=e(1+s)P_i^3\delta_{ij}-\left[s-ed\gamma-e\left(\omega^2-\gamma^2\right)-(1+s)r\left(\omega^2-\gamma^2\right)\right]P_{i,j}^2 \\ &-\left[\gamma d+\left(\omega^2-\gamma^2\right)\right]P_i^1\delta_{ij}-m\left(\omega^2-\gamma^2\right)\sum_{k=1}^{nm}\left[\Gamma_{i,j}(\xi_k)\right], \end{aligned} \tag{15}$$

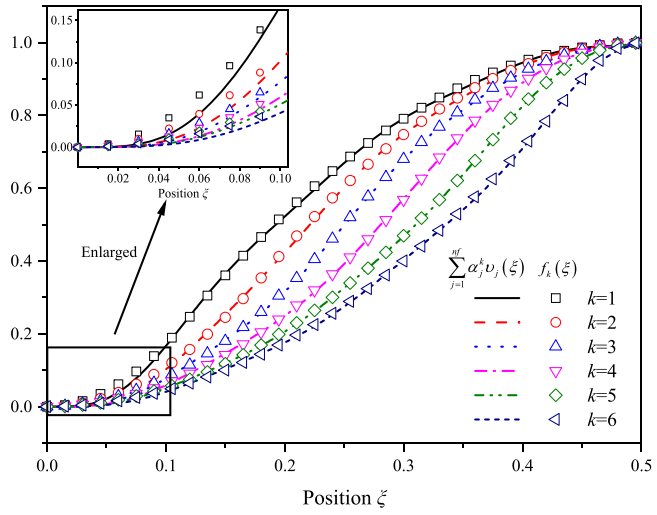

Fig. 2. The fitting results of the transformed function $\sum_{j=1}^{nf}\alpha_j^k\upsilon_j(\xi)$ and the objective function $f_k(\xi)$ for different k.

$$Y_{i,j}=[ed-2e\gamma-2(1+s)r\gamma]P_{i,j}^2-(d-2\gamma)P_i^1\delta_{ij}+2\gamma m\sum_{k=1}^{nm}\left[\Gamma_{i,j}(\xi_k)\right]. \tag{16}$$

where j_0= 1 and thus i=1, 2, ⋯, ns; j=1, 2, ⋯, ns. Here, δ_{ij} is the Kronecker delta and the constants are expressed as follows:

$$P_i^1=\int_0^1\widehat{\phi}_i\widehat{\phi}_i\mathrm{d}\xi,\quad P_{i,j}^2=\int_0^1\widehat{\phi}_i\frac{\mathrm{d}^2\widehat{\phi}_j}{\mathrm{d}\xi^2}\mathrm{d}\xi,\quad P_i^3=\int_0^1\widehat{\phi}_i\frac{\mathrm{d}^4\widehat{\phi}_i}{\mathrm{d}\xi^4}\mathrm{d}\xi,\quad \Gamma_{i,j}(\xi)=\widehat{\phi}_i(\xi)\left[\widehat{\phi}_j(\xi)-c\frac{\mathrm{d}^2\widehat{\phi}_j(\xi)}{\mathrm{d}\xi^2}\right]. \tag{17}$$

The nontrivial solution of the Eq. (14) are obtained by solving the following equations, which sets the matrix determinant zero:

$$\det[\mathbf{X}(\omega,\gamma)]=0,\quad \det[\mathbf{Y}(\gamma)]=0, \tag{18}$$

where the det(·) is the determinant of the matrix.

It is assumed that the small attached mass m has little impact on the mode shape $\widehat{\phi}_j(\xi)$. When the beam is resonant in the j-th mode, the amplitude a_j of that mode is exceedingly larger than the others. The following approximate analytical solutions are obtained by neglecting the non-diagonal elements in Eq. (18) [33], which is same as the stage of ns= 1 and j_0=j:

$$\gamma_j=\frac{d}{2}\frac{P_j^1-eP_{j,j}^2}{P_j^1-[e+(1+s)r]P_{j,j}^2+m\sum_{k=1}^{nm}\left[\Gamma_{j,j}(\xi_k)\right]}, \tag{19}$$

where the γ_j and ω_j are the decay rate and resonant frequency of the j-th mode respectively.

There are two stages to obtain the solution of the present model: (1) By using the single mode shape, namely ns= 1, the solution is expressed as Eqs. (19) and (20); (2) By using the multiple mode shapes, namely ns> 1, the solution is obtained through the computation of Eq. (18) and the starting mode number j_0 is usually set as one.

From Eq. (19), the adding mass on beam can reduce the decay rate γ_j, even though the dimensionless damping factor d keeps unchanged. This phenomenon can be explained by the single degree of freedom (SDOF) model: When the system is in underdamping oscillation, the decay rate γ of the viscously damped SDOF system is γ=d/2m [48]. Apparently, when the mass of an SDOF system increases, the decay rate γ decreases.

In the present model, from Eq. (19), the relation between the quality factor and the added mass is given as follows:

$$\frac{Q_j}{Q_{j,0}}=\frac{\omega_j}{\omega_{j,0}}\left\{1+m\frac{\sum_{k=1}^{nm}\left[\Gamma_{j,j}(\xi_k)\right]}{P_j^1-[e+(1+s)r]P_{j,j}^2}\right\}. \tag{21}$$

where the $\omega_{j,0}$ and $Q_{j,0}$ are the resonant frequency and quality factor of the unloaded beam, respectively.

The similar mass effect on the quality factor is also given as follows [49–51]:

$$\frac{Q_j}{Q_{j,0}}=(1+m)\frac{\mathrm{Im}\Theta(\omega_j)}{\mathrm{Im}\Theta(\omega_{j,0})}, \tag{22}$$

where Θ is the known hydrodynamic function for the mass resonator [50]. These results imply that measuring the shifts of decay rate γ_j in different order resonance can be used to detect the mass of particles on beam. The damping characteristics have been studied on the mass identification [52] and the crack detection on beams [53].

Moreover, as the damping coefficient d increases, the resonant frequency ω_j decreases as indicated by Eq. (20). The influence of damping should be considered for the change of resonant frequency after the attachment of particles.

3. Mass identification of particles on doubly clamped beam

In conjunction with Eqs. (19) and (20), the relationship between the resonant frequency with attached masses is derived as follows:

$$\frac{\omega_{j,0}^2+\gamma_{j,0}^2}{\omega_j^2+\gamma_j^2}-1=\frac{m\sum_{i=1}^{nm}\left[\Gamma_{j,j}(\xi_i)\right]}{P_j^1-[e+(1+s)r]P_{j,j}^2}, \tag{23}$$

where $\gamma_{j,0}$ denotes the decay rate with no attached particles on beam.

From Eq. (23) this result can be reduced to a simpler formula in the

$$\omega_j=\sqrt{\frac{e(1+s)P_j^3-sP_{j,j}^2}{P_j^1-[e+(1+s)r]P_{j,j}^2+m\sum_{k=1}^{nm}\left[\Gamma_{j,j}(\xi_k)\right]}-\frac{d^2\left(P_j^1-eP_{j,j}^2\right)^2}{4\left\{P_j^1-[e+(1+s)r]P_{j,j}^2+m\sum_{k=1}^{nm}\left[\Gamma_{j,j}(\xi_k)\right]\right\}^2}}. \tag{20}$$

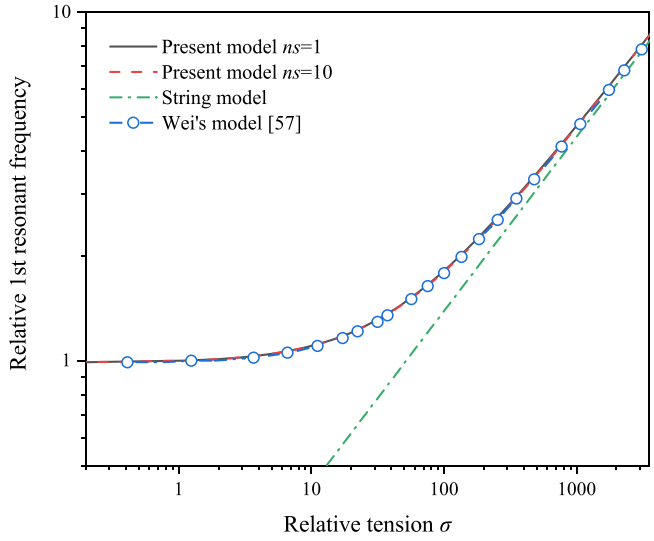

Fig. 3. The relative first resonant frequency versus the relative tension σ in the present model, the string model, and Wei's model [57].

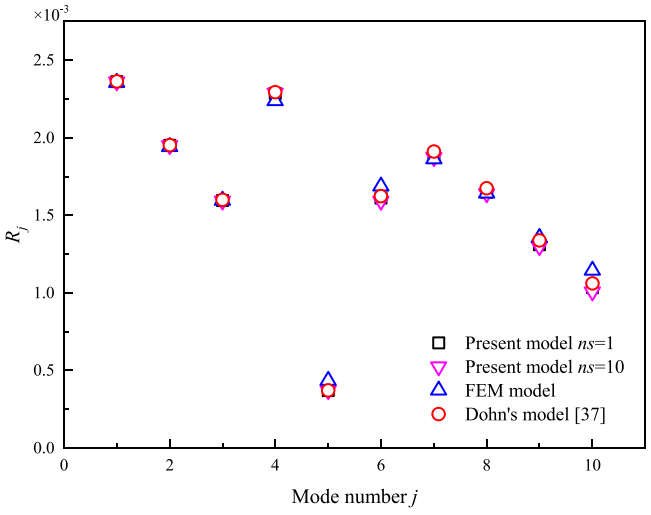

Fig. 4. The comparison of R_j computed by the present model, FEM model and Dohn's model [37].

Euler-Bernoulli beam model, which has been obtained in the research [37], expressed as follows:

$$\frac{\omega_{j,0}^2}{\omega_j^2} - 1 = \frac{m}{P_j^1}\sum_{i=1}^{nm}[\widehat{\phi}_i(\xi_i)]^2. \tag{24}$$

But it should be mentioned that the consideration of the damping effect and the Timoshenko beam theory improves the mass sensing precision, which is more suitable for a high-order resonance.

Now Eq. (23) is written as the following form:

$$R_j = m\sum_{i=1}^{nm} v_j(\xi_i), \tag{25}$$

where the indicator R_j and function $v_j(\xi)$ are expressed as:

$$R_j = \frac{\omega_{j,0}^2 + \gamma_{j,0}^2}{\omega_j^2 + \gamma_j^2} - 1, \quad v_j(\xi) = \frac{\Gamma_{j,j}(\xi)}{P_j^1 - [e + (1+s)r]P_{j,j}^2}. \tag{26}$$

In Eq. (25), the relationship between the indicator R_j and m is linear, where R_j can be easily obtained from the frequencies and decay rates before and after the particles attachments. However, the relationship between R_j and ξ_i is nonlinear, due to the oscillation characteristics of model shape function ϕ_j. This brings difficulties to determine particles masses and positions. It should be noted that the variable range is $\xi \in [0, 1/2]$ in this inversion process, for the function $v_j(\xi)$ is symmetrical to the axis $\xi = 1/2$, which is $v_j(\xi) = v_j(1-\xi)$, owing to the symmetrical properties of the doubly clamped beam. So when the estimated position ξ_i is obtained after computation, the position $1 - \xi_i$ is also the (possible) position in this identification. Compared with the indicator of frequency shifts in [37], the influence of damping effect is included in the present R_j.

In order to break the restriction of initial guess in the inversion algorithm computation, we employ an approximation of transformation on the function, whose effect is to replace the oscillation function $v_j(\xi)$ with a monotonic one $f_k(\xi)$ when the positions of particles ξ_i change in the iteration steps. The transformation parameters are determined from the least-squares analysis as follows [30]:

$$L\left(\alpha_j^k\right) = \int_0^{\frac{1}{2}}\left[\sum_{j=1}^{nf}\alpha_j^k v_j(\xi) - f_k(\xi)\right]^2 \mathrm{d}\xi, \tag{27}$$

where nf is the number of frequencies in this mass identification process and the object function $f_k(\xi)$ is defined as a series of two-segmented parabolic functions, expressed as follows:

$$f_k(\xi) = \begin{cases} \left[\dfrac{2}{\zeta_k(1-2\zeta_k)} - \dfrac{4}{1-2\zeta_k}\right]\xi^2, & (0 \le \xi \le \zeta_k) \\ -\dfrac{4}{1-2\zeta_k}\xi^2 + \dfrac{4}{1-2\zeta_k}\xi + 1 - \dfrac{1}{1-2\zeta_k}, & (\zeta_k < \xi \le 1/2) \end{cases} \tag{28}$$

where ζ_k is defined with a given nf as follows:

$$\zeta_k = 0.05 + \frac{0.4}{nf}k, \qquad k = 1, 2, 3, \ldots, nf. \tag{29}$$

With different k in Eq. (29), ζ_k should be sparsely distributed. When the two ζ_k are close, the values of $f_k(\xi)$ are also close, which leads to very large numerical error in the computation of inversing the Jacobian matrix in iteration.

The solution α_j^k of the minimum optimization problem of Eq. (27) is shown in the matrix form:

$$\boldsymbol{\alpha} = \mathbf{A}^{-1}\mathbf{B}, \tag{30}$$

where $\boldsymbol{\alpha}$, $\mathbf{A}$ and $\mathbf{B}$ are the $nf \times nf$ matrices; The expressions of $\mathbf{A}$ and $\mathbf{B}$ are given as follows:

$$A_{kj} = \int_0^{\frac{1}{2}} v_k(\xi)v_j(\xi)\mathrm{d}\xi, \quad B_{kj} = \int_0^{\frac{1}{2}} f_k(\xi)v_j(\xi)\mathrm{d}\xi. \tag{31}$$

In Fig. 2, the fitting results versus different position, which are calculated by the least-squares method of Eq. (27) with $nf = 6$, are displayed, where the curves denote $\sum_{j=1}^{nf}\alpha_j^k v_j(\xi)$ and symbols denote $f_k(\xi)$. The fitting results are in excellent agreement with most positions. However, as seen in the enlarged graph when position $\xi < 0.1$, the error is rather obvious, and the similar observations are also reported [30].

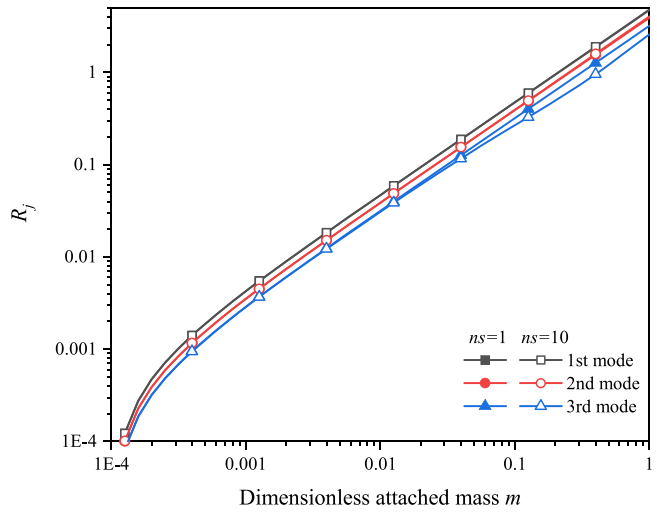

Fig. 5. The comparison of the R_j computed with ns= 1 and ns= 10, as the function of the attached mass m.

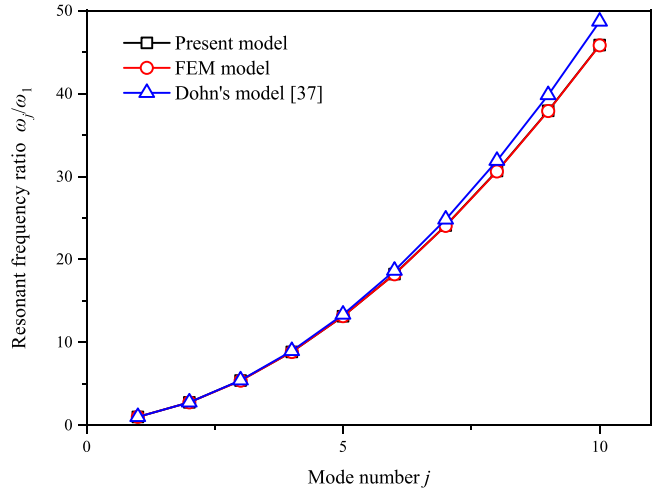

Fig. 6. The comparison of the resonant frequency ratio of ω_j/ω_1 as the function of the mode number. Here three ratios of ω_j/ω_1 are computed by the present model, FEM model and Dohn's model [37].

Eq. (25) can also be written in the following vector form:

$$\mathbf{R} = m\mathbf{U}, \tag{32}$$

where the vectors **R** and **U** are

$$\mathbf{R} = \left[R_1, \ldots, R_j, \ldots, R_{nf}\right]^{\mathrm{T}}, \quad \mathbf{U} = \left[\sum_{i=1}^{nm} \upsilon_1(\xi_i), \ldots, \sum_{i=1}^{nm} \upsilon_j(\xi_i), \ldots, \sum_{i=1}^{nm} \upsilon_{nf}(\xi_i)\right]^{\mathrm{T}}. \tag{33}$$

In conjunction with Eqs. (27) and (32), the following approximation is obtained by

$$\boldsymbol{\alpha}^{\mathrm{T}}\mathbf{R} = m\boldsymbol{\alpha}^{\mathrm{T}}\mathbf{U} \approx m\mathbf{f}, \tag{34}$$

where **f** is the vector of the monotonic functions defined as follows:

$$\mathbf{f} = \left[\sum_{i=1}^{nm} f_1(\xi_i), \ldots, \sum_{i=1}^{nm} f_j(\xi_i), \ldots, \sum_{i=1}^{nm} f_{nf}(\xi_i)\right]^{\mathrm{T}}. \tag{35}$$

Defining the vector $\mathbf{TR}=\boldsymbol{\alpha}^{\mathrm{T}}\mathbf{R}$ and the estimated variable vector $\boldsymbol{\theta}= [m, \xi_1, \xi_2, \cdots, \xi_{nm}]^{\mathrm{T}}$, the sensitivity matrix $\mathbf{D}= \partial(\mathbf{TR})/\partial\boldsymbol{\theta}$, which is also the Jacobian matrix, is given as:

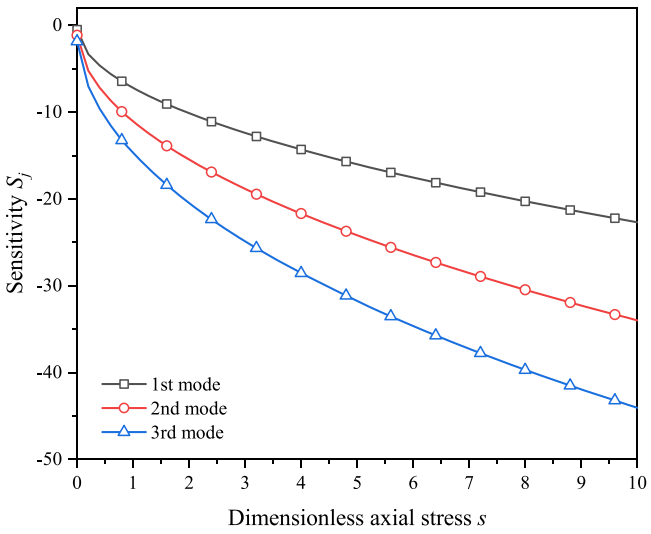

Fig. 7. The sensitivity S_j of the Timoshenko beam model and string vibration model versus the dimensionless axial tension s.

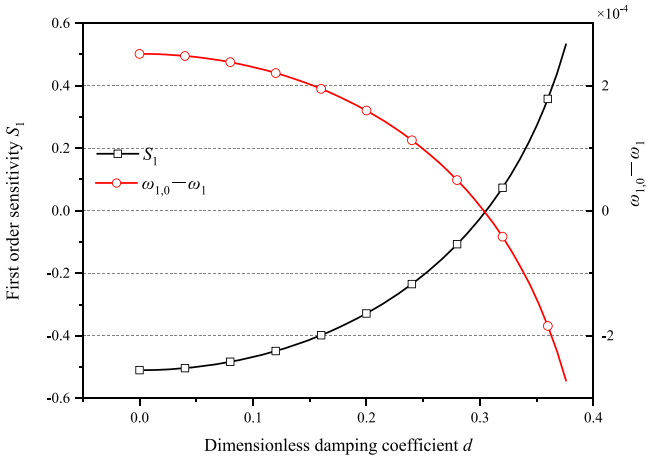

Fig. 8. The influences of dimensionless damping coefficient d on the sensitivity S_1 and $\omega_{1,0}$ - ω_1. Here, ω_1 and $\omega_{1,0}$ are the first natural frequencies with and without the attached mass.

$$\mathbf{D}(\boldsymbol{\theta}) = \frac{\partial(\mathbf{TR})}{\partial\boldsymbol{\theta}} = \begin{bmatrix} \sum_{i=1}^{nm} f_1(\xi_i) & mf_1'(\xi_1) & mf_1'(\xi_2) & \cdots & mf_1'(\xi_{nm}) \\ \sum_{i=1}^{nm} f_2(\xi_i) & mf_2'(\xi_1) & mf_2'(\xi_2) & \cdots & mf_2'(\xi_{nm}) \\ \vdots & \vdots & \vdots & & \vdots \\ \sum_{i=1}^{nm} f_{nf}(\xi_i) & mf_{nf}'(\xi_1) & mf_{nf}'(\xi_2) & \cdots & mf_{nf}'(\xi_{nm}) \end{bmatrix}, \tag{36}$$

where the $f_k'(\xi)$ denotes $\mathrm{d}f_k(\xi)/\mathrm{d}\xi$, for k=1, 2, ⋯, nf. In order to obtain the estimated value of $\boldsymbol{\theta}^{est}$, based on the Levenberg-Marquardt algorithm [54,55], the following iteration process is introduced:

$$\boldsymbol{\theta}_{k+1} = \boldsymbol{\theta}_k + \mu_k \cdot \left(\mathbf{D}_k^{\mathrm{T}}\mathbf{D}_k + \lambda_k\mathbf{I}\right)^{-1}\mathbf{D}_k^{\mathrm{T}}(\mathbf{TR}_{obs} - \mathbf{TR}_k), \quad k = 0,\ 1,\ 2,\ \cdots N_{\max}, \tag{37}$$

where the subscripts of k and obs denote the k-th iteration and the observed value, respectively. **I** is the identity matrix. The damping

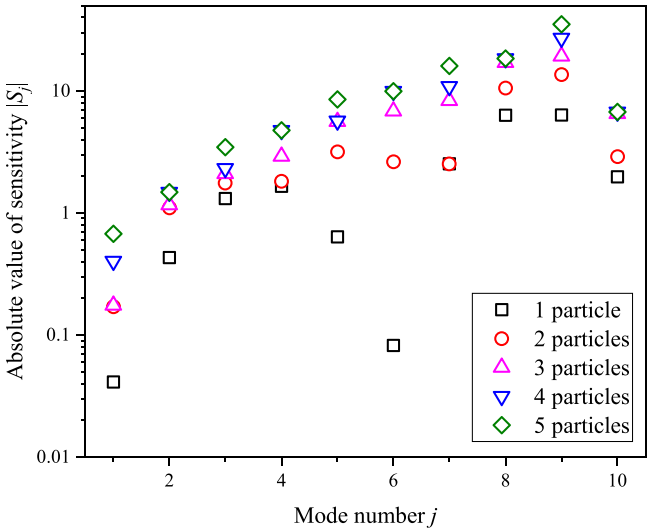

Fig. 9. The absolute values of sensitivity $|Sj|$ versus the mode number. There are five scenarios with five different particles. They are one particle with ξ_1= 0.2; two particles with ξ_1= 0.2 and ξ_2= 0.3; three particles with ξ_1= 0.1, ξ_2= 0.2 and ξ_3= 0.3; four particles with ξ_1= 0.1, ξ_2= 0.2, ξ_3= 0.3 and ξ_4= 0.4; five particles with ξ_1= 0.1, ξ_2= 0.2, ξ_3= 0.3, ξ_4= 0.4 and ξ_5= 0.5.

factors of this algorithm, μ_k and λ_k, are evaluated as $\mu_k < 1$ and $10^{-10} < \lambda_k < 10^{-7}$ based on experience. The term $\lambda_k\mathbf{I}$ is important for this algorithm, for it can mitigate the ill-conditions of the Hessian matrix $\mathbf{D}_k^T\mathbf{D}_k$ and avoid the numerical errors in the matrix inversion process. $N_{\max}$ is the iteration end point. $\mathbf{TR}_k=\boldsymbol{\alpha}^T\mathbf{R}_k$, where $\mathbf{R}_k$ is computed by Eq. (32) and $\boldsymbol{\theta}_k$. The initial guess is represented as $\boldsymbol{\theta}_0$. According to the reference [25], the term $\lambda_k\mathbf{I}$ can be replaced with the covariance matrix, which has been utilized in the mass identification [56].

By repeating the iteration of Eq. (37), the estimated $\boldsymbol{\theta}^{estimate}=\boldsymbol{\theta}_{k+1}$ is obtained at the last iteration. In order to ensure the validity of the mass identification algorithm, the number of particles should be less than the number of measured frequencies, which is $nm<nf$.

The flowcharts of the frequency shifts prediction and mass identification are shown in Appendix. B.

4. Results and discussion on frequency shifts prediction

4.1. Validation of the frequency shifts

In this study, the beam material is silicon, with Young's modulus of E=169 GPa, mass density of ρ=2330 kg/m^3 and Poisson's ratio of ν=0.2. The beam length is l= 500 μm, the width is b= 50 μm and the thickness is h=10 μm.

In order to investigate the influence of the axial load on the resonant frequency, Fig. 3 shows the first relative resonant frequency $\overline{\omega}_1$ as the function of the relative tension σ. Here $\overline{\omega}_1 = \omega_1/\omega_1^0$, $\omega_1^0=\omega_1$ at σ=1 and $\sigma=s/e=Tl^2/EI$. In the figure, the dimensionless attached mass m and the dimensionless damping coefficient d are neglected. In Fig. 3, the curves show the results of present model with ns= 1 as Eq. (20), the results of present model with ns= 10 in Eq. (18) and the results of the string model. Especially, the results of the string model are computed as ω_1^s/ω_1^0, where $\omega_j^s = \sqrt{j^4\pi^4 e + j^2\pi^2 s}$ for j=1, 2, 3 ⋯. The line with circles is the result taken from the previous research [57], which has been validated by the experiments. The results of the beam model all approach to those of the string model as the increase of σ. The results with ns= 1 are in good agreement with those with ns= 10, which indicates the computation of Eq. (20) is accurate. The agreement on the results of the present model and Wei's results [57] validates our model incorporating the axial load effect. It should be noted that the result

Table 1
The estimated values with the mass identification process and the exact values of the mass and positions of particles. The input resonant frequency values are computed by the present model, from the given mass and positions in the exact values.

		Mass m	ξ_1	ξ_2	ξ_3	ξ_4	ξ_5
2 particles	Exact	1.5×10^{-3}	0.24	0.46			
	Estimated (nf=6)	1.5000×10^{-3}	0.24000	0.46000			
	Error	0.00%	0.00%	0.00%			
	Exact	1.5×10^{-3}	0.24	0.24			
	Estimated (nf=6)	1.5000×10^{-3}	0.24004	0.23996			
	Error	0.00%	0.02%	-0.02%			
3 particles	Exact	5×10^{-3}	0.18	0.25	0.38		
	Estimated (nf=6)	5.000×10^{-3}	0.18000	0.25000	0.37999		
	Error	0.00%	0.00%	0.00%	0.00%		
	Exact	8×10^{-3}	0.25	0.42	0.45		
	Estimated (nf=6)	7.992×10^{-3}	0.25016	0.42457	0.44474		
	Error	-0.10%	0.06%	1.09%	-1.17%		
4 particles	Exact	1×10^{-2}	0.15	0.28	0.3	0.41	
	Estimated (nf=6)	0.995×10^{-2}	0.15214	0.28771	0.28772	0.42479	
	Error	-0.50%	1.43%	2.75%	-4.09%	3.61%	
	Exact	0.02	0.15	0.19	0.23	0.31	
	Estimated (nf=6)	0.02000	0.14994	0.19006	0.22995	0.31001	
	Error	0.00%	-0.04%	0.03%	-0.02%	0.00%	
5 particles	Exact	1×10^{-3}	0.08	0.15	0.24	0.29	0.35
	Estimated (nf=6)	0.907×10^{-3}	0.11331	0.17370	0.26701	0.28545	0.35557
	Error	-9.30%	41.64%	15.80%	11.25%	-1.57%	1.59%
	Estimated (nf=10)	1.000×10^{-3}	0.08000	0.15000	0.24000	0.29000	0.35000
	Error	0.00%	0.00%	0.00%	0.00%	0.00%	0.00%
	Exact	8×10^{-3}	0.09	0.18	0.35	0.42	0.48
	Estimated (nf=6)	8.146×10^{-3}	0.08125	0.17330	0.36647	0.39985	0.43324
	Error	1.83%	-9.72%	-3.72%	4.71%	-4.80%	-9.74%
	Estimated (nf=10)	7.984×10^{-3}	0.09141	0.18018	0.35434	0.41318	0.49791
	Error	-0.20%	1.57%	0.10%	1.24%	-1.62%	3.73%

Table 2
The estimated values with the mass identification process, the exact values and the errors of the mass and positions of particles. The input resonant frequency values are computed by the present model, from the given mass and positions in the exact values.

		Mass m	ξ_1	ξ_2	ξ_3	ξ_4	ξ_5
3 particles	Exact	5×10^{-4}	0.221	0.376	0.424		
	Estimated (nf=6)	5.016×10^{-4}	0.21941	0.36921	0.43471		
	Error	0.32%	-0.72%	-1.81%	2.53%		
4 particles	Exact	5×10^{-4}	0.111	0.146	0.274	0.341	
	Estimated (nf=6)	4.999×10^{-4}	0.11006	0.14619	0.27003	0.34306	
	Error	-0.03%	-0.84%	0.13%	-1.45%	0.61%	
5 particles	Exact	5×10^{-4}	0.071	0.254	0.271	0.326	0.490
	Estimated (nf=6)	4.963×10^{-4}	0.07193	0.23770	0.29455	0.31174	0.49723
	Error	-0.74%	1.31%	-4.37%	8.69%	-6.42%	1.48%

gives a more general description of the frequency variation with σ. The reason is that the eigenvalues of g_j^1 and g_j^2 in the mode shapes of Eq. (13) are only influenced by the relative tension σ.

To confirm the validation of present model, the scenario of three masses attached on the beam is considered, in which the relative mass m is 0.0005, and locations ξ_is are 0.224, 0.376 and 0.576. In this case, the axial load T and damping coefficient D are both assumed to be zero. From Eq. (26), R_j reflects the frequency shifts resulting from the attached mass particles. Fig. 4 displays the R_j obtained by the present model with ns= 1 and ns= 10, Dohn's model [37] and FEM model. The results of the present model with ns= 1 and ns= 10 are almost the same, which verifies the accuracy of the computation by Eq. (20). All four results in Fig. 4 are very close to one another.

The approximation solutions in Eqs. (19) and (20) are based on the assumption that the mode shape hardly changes after the adsorption of the particles. But the attachment of the particles may cause small changes of the mode shapes [58]. The influence of the attached mass m on R_j is investigated in Fig. 5. The damping effect is neglected and three particles are added on the beam with locations ξ_i are 0.224, 0.376 and 0.576. In the figure, the values of R_j computed by the two different ns of 1 and 10 are separated when m increases. Actually, the attachment of the particle may be regarded as a sudden jump of the shear force at the local position. The difference between the two values of R_j calculated by two methods enlarges when m increases. This phenomenon is also discussed in [34], where the position of the particle affects this difference. However, the difference in the present model is much smaller, for the formula of R_j is suitable to draw a linear relationship with m. Accordingly, as m is usually very small in the practical applications of mass resonators, the result by ns= 1 is accurate.

In Fig. 6, the results of ω_j/ω_1 (ratio of the j-th resonant frequency to

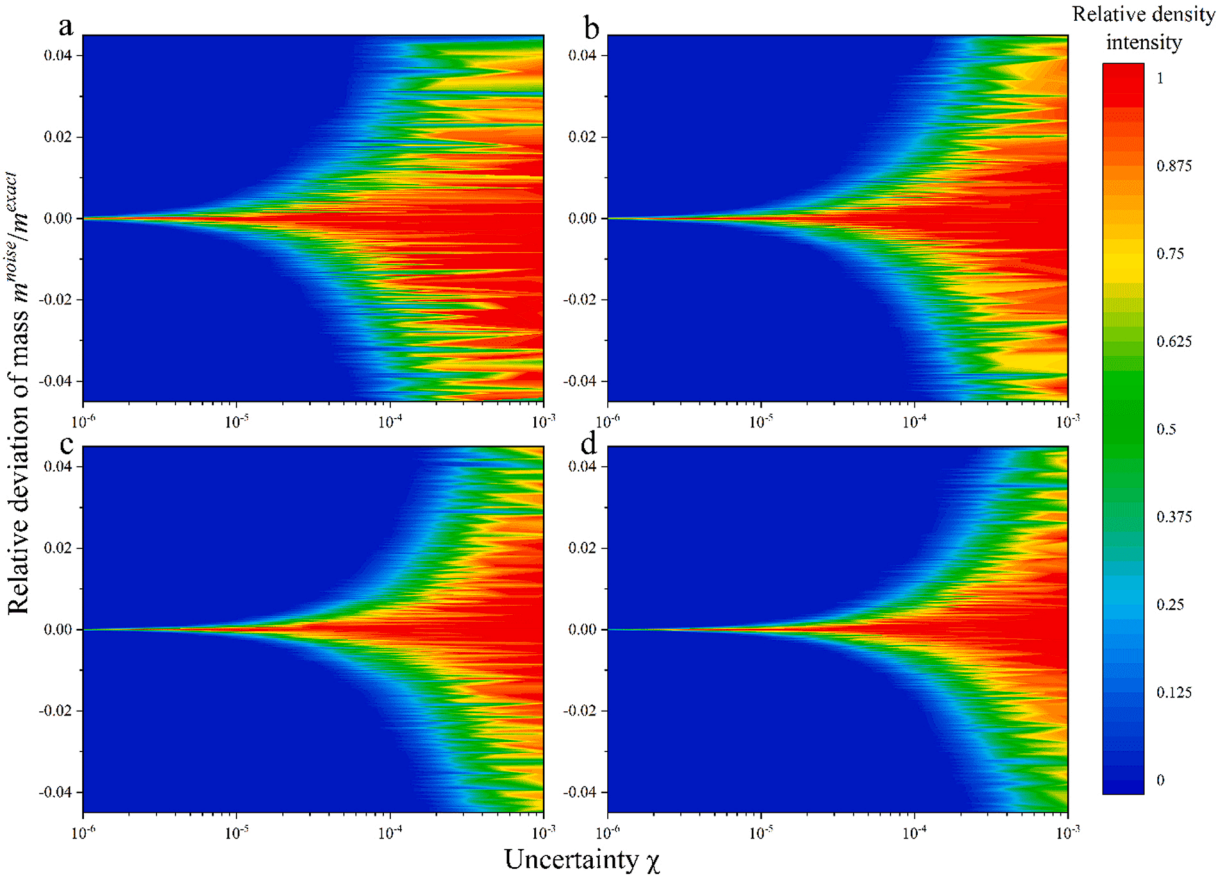

Fig. 10. Relative density of the relative deviation of mass m^{noise}/m^{exact} variating with uncertainty χ, for (a) one particle with position ξ_1= 0.2; (b) two particles with position ξ_1= 0.2 and ξ_2= 0.3; (c) three particles with position ξ_1= 0.2, ξ_2= 0.3 and ξ_3= 0.4; (d) four particles with position ξ_1= 0.2, ξ_2= 0.3, ξ_3= 0.4 and ξ_4= 0.45.

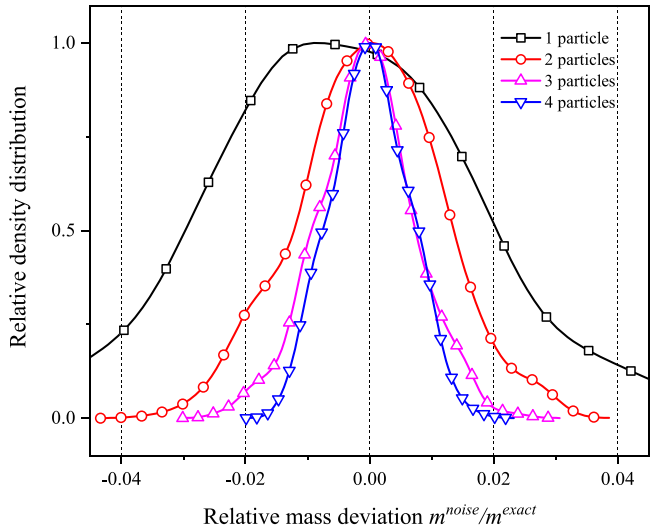

Fig. 11. Relative density of the mass deviation with different particle number, when with the uncertainty of χ=10^{-4}.

the first) by the present model, FEM and Dohn's model are compared. The curves with squares, circles and triangles in Fig. 6 denote the results of the present model with *ns*= 1, FEM and Dohn [37]. It can be seen that the three curves are almost overlapping when the mode number $j \leq 5$. When $j > 5$, the result of Dohn's model deviates rather significantly from the other curves, because the Euler-Bernoulli model is used in Dohn's model. The prediction of the present model keeps consistent with that of the FEM model. The shearing effect in the Timoshenko beam model softens a beam structure, which leads to the smaller resonant frequency.

4.2. The mass resonator sensitivity

The sensitivity S_j, which is also called the responsivity, is defined as the changing rate of the resonant frequency with respect to the attached mass m [6,59], where the subscript j is the mode number. To investigate this, by using the first order approximation, the sensitivity S_j is calculated as follows:

$$S_j = \frac{\partial \omega_j}{\partial m} \approx -\frac{\sum_{i=1}^{nm} v_j(\xi_i)}{2\omega_{j,0}} \left\{ \frac{e(1+s)P_j^3 - sP_{j,j}^2}{P_j^1 - [e+(1+s)r]P_{j,j}^2} - \frac{d^2\left(P_j^1 - eP_{j,j}^2\right)^2}{2\left\{P_j^1 - [e+(1+s)r]P_{j,j}^2\right\}^2} \right\}. \tag{38}$$

The S_j variation of the first three modes as the function of the axial load is presented in Fig. 7. The dimensionless damping coefficient d= 0 and three particles are assumed to be located at 0.224, 0.376 and 0.576. Based on Fig. 7, the sensitivities are all negative, because adding a mass increases the inertial effect and reduces the resonant frequency. The absolute values of sensitivities S_j keep increasing with the increase of axial tension s and also the mode number, which shows that the additional tension enhances the sensitivity of mass sensors [33,60].

The damping factor d also affects sensitivity S, which is shown in Fig. 8. From the curve with squares in the figure, with the increase of d, the sensitivity S_1 changes from negative to positive. However, its absolute value firstly decreases and then increases. This interesting phenomenon is shown by the curve with the circle symbol, which denotes the difference of resonant frequencies without and with the attached mass m= 0.0005. The sensitivity S_j is positive, when the resonator is in the strong damping effect, expressed as:

$$d > \frac{\sqrt{2\left[e(1+s)P_j^3 - sP_{j,j}^2\right]\left\{P_j^1 - [e+(1+s)r]P_{j,j}^2\right\}}}{P_j^1 - eP_{j,j}^2}. \tag{39}$$

This is opposite to the results in low damping environment. The reason is that when the decrease of γ, caused by the attached mass, overcomes the mass effect on the resonant frequency reduction, the resonant frequency will increase after the attachment of mass particles. In general, the variation of decay rate γ should not be ignored.

As shown in Fig. 9, the absolute values of sensitivities $|S_j|$ versus mode number are presented. In this case, the zero axial load and damping coefficient are assumed. Here, there are five scenarios: one particle with ξ_1= 0.2; two particles with ξ_1= 0.2 and ξ_2= 0.3; three particles with ξ_1= 0.1, ξ_2= 0.2 and ξ_3= 0.3; four particles with ξ_1= 0.1, ξ_2= 0.2, ξ_3= 0.3 and ξ_4= 0.4; five particles with ξ_1= 0.1, ξ_2= 0.2, ξ_3= 0.3, ξ_4= 0.4 and ξ_5= 0.5. In Fig. 9, the sensitivity is dependent on the mode number: Higher mode number leads to a higher sensitivity [11]. The inertial effect caused by the attached mass increases with the increase of the natural frequency of a mass resonator. For the scenario of only one particle in Fig. 9, the absolute values of sensitivities on the fifth and sixth modes rapidly descend. The reason is that vibration amplitudes of the fifth and sixth modes are smaller than that of the fourth mode, at the particle position ξ=0.2. However, as to five-particle scenario, the absolute values of sensitivities keep increasing, except for the tenth mode. In the application of mass sensors, the particles land randomly on the beam surface, which implies the multi-particles may avoid the sudden decrease of sensitivity in a certain mode. In general, the absolute values of sensitivities are increasing with the adding of particles, except for the cases that the added particles are sited on the nodes, whose vibration amplitude is zero.

4.3. The validation on mass sensing process

In the inverse process to estimate the attached mass m shown as Eq. (37), we try to solve the following question:

$$TR_j = m^{estimate} \sum_{i=1}^{nm} f_j(\xi_i), \tag{40}$$

where $m^{estimate}$ denotes the estimated mass from the inverse computation. From the exact expression in Eq. (25) and the transformation $TR_j = \sum_{k=1}^{nf} \alpha_k^j R_k$, then by exchanging the order of summation, the relationship between estimated mass $m^{estimate}$ and the exact mass m^{exact} is expressed as:

$$m^{exact} \sum_{i=1}^{nm} \sum_{k=1}^{nf} \alpha_k^j v_k(\xi_i) = m^{estimate} \sum_{i=1}^{nm} f_j(\xi_i). \tag{41}$$

So the estimated mass $m^{estimate}$ can be calculated as:

$$m^{estimate} = m^{exact} \frac{\sum_{i=1}^{nm} \sum_{k=1}^{nf} \alpha_k^j v_k(\xi_i)}{\sum_{i=1}^{nm} f_j(\xi_i)}. \tag{42}$$

The accuracy of this estimation process depends on the approximation of the least-squares in Eq. (27). When *nf* increases in this approximation, the value of $m^{estimate}$ may be estimated more accurately.

The estimation results are presented in Table 1. The frequencies shift results R_j are computed by the present Timoshenko beam model. At the estimated rows, the results are obtained by two situations: *nf*= 6 and *nf*= 10. From the table, when two or three particles are involved in the

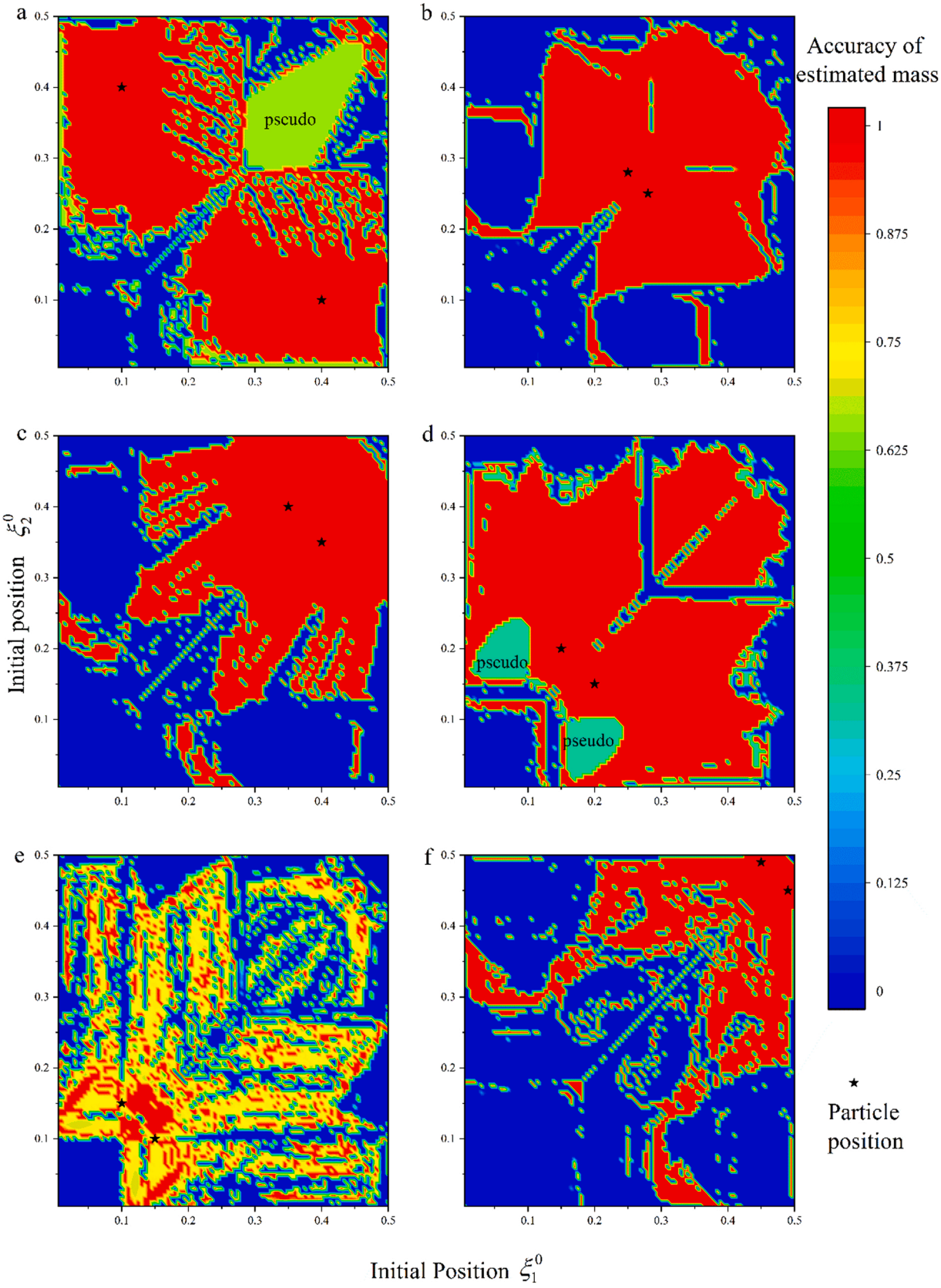

Fig. 12. Influence of different initial (guessed) positions on the accuracy of the mass estimation in the iteration process. Here the particle number is two, and six modes, i.e., *nf*= 6, are used. The particle positions are marked by the symbols of star: (a) ξ_1^{exact}= 0.1, ξ_2^{exact}= 0.4; (b) ξ_1^{exact}= 0.25, ξ_2^{exact}= 0.28; (c) ξ_1^{exact}= 0.35, ξ_2^{exact}= 0.4; (d) ξ_1^{exact}= 0.15, ξ_2^{exact}= 0.2; (e) ξ_1^{exact}= 0.1, ξ_2^{exact}= 0.15; (f) ξ_1^{exact}= 0.45, ξ_2^{exact}= 0.49.

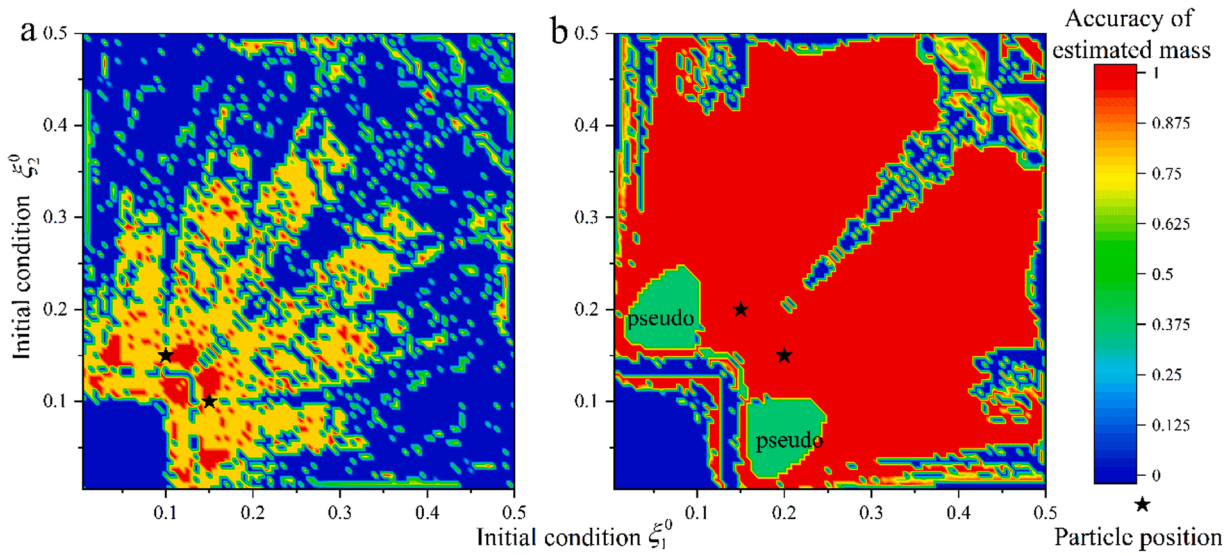

Fig. 13. Influence of different initial (guessed) positions on the accuracy of the mass estimation in the iteration process. Here the particle number is two, and ten modes, i.e., nf= 10, are used. The particle positions are marked by symbols of star: (a) ξ_1^{exact}= 0.1, ξ_2^{exact}= 0.15; (b) ξ_1^{exact}= 0.15, ξ_2^{exact}= 0.2.

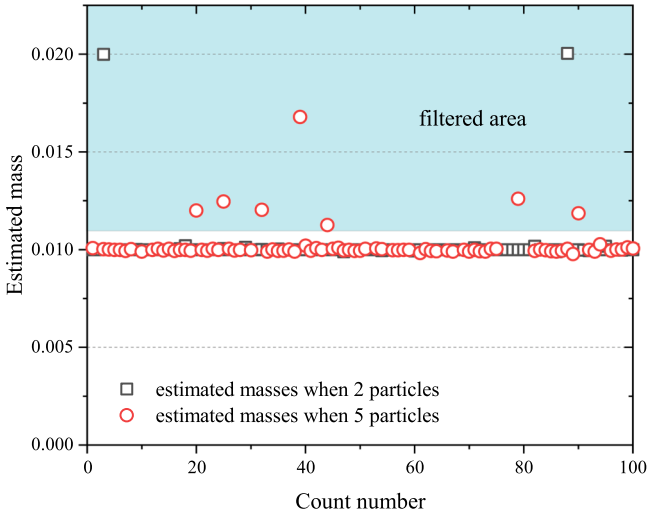

Fig. 14. The Estimated masses at the scenarios with 2 particles and 5 particles, for nf= 6.

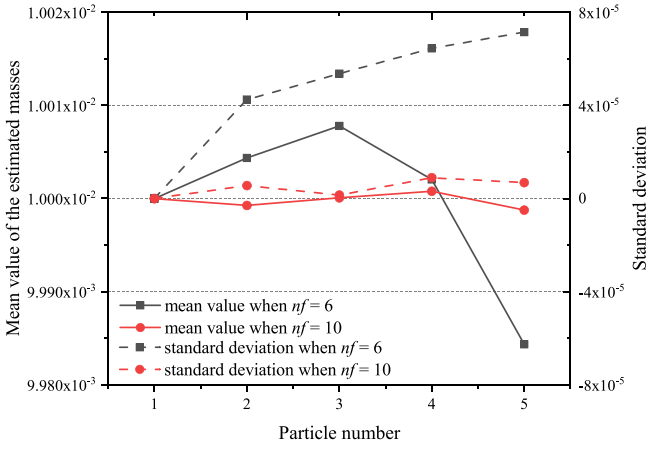

Fig. 15. The mean values and standard deviations of the estimated masses after the results filter, at the scenarios with frequency number nf= 6 and 10, and particle number nm= 1, 2, 3, 4 and 5.

mass identification, the estimated values are in good agreement with the exact ones. For the four-particle scenario, the estimated mass m is obviously more accurate than the estimated positions of particles. The reason is that the frequency shift is more dependent on particle position rather than on the particle mass, which leads to a higher anti-noise ability on mass identification. For 5 particles, increasing the number of resonant frequencies can remarkably improve the precision of estimation.

By using the input resonant frequencies computed by FEM model, the estimated values and errors from the inversion process are presented in Table 2, where six frequencies are used in the inversion process. For the different results between the present model and FEM model illustrated in Fig. 4, the accuracy of mass identification may be affected. However, after the inversion process, the attached masses have been identified successfully. Obviously from Table 2, the error of mass m is smaller than that of particle locations ξ_i, which is similar with Table 1.

4.4. The noise effect on mass identification

Maintaining the numerical stability of the mass identification algorithm is important for a broad application, for the measuring noise in certain frequencies range cannot be eliminated. To investigate the robustness, we assume a small quantity of noise value on the imported frequency shifts and the estimated mass and positions, expressed as

$$R_j = R_j^{exact} + R_j^{noise}, \quad m = m^{exact} + m^{noise}, \quad \xi_i = \xi_i^{exact} + \xi_i^{noise}, \tag{43}$$

where the superscripts of *exact* and *noise* denote the exact value and noise value, respectively. Because the noise contribution to the

frequency shift is (assumed) rather small, by substituting Eq. (43) into Eq. (25), following equation is assumed to be true:

$$R_j^{exact} + R_j^{noise} = \left(m^{exact} + m^{noise}\right) \sum_{i=1}^{nm} v_j\left(\xi_i^{exact} + \xi_i^{noise}\right). \tag{44}$$

Then by substituting the exact solution $R_j^{exact} = m^{exact} \sum_{i=1}^{nm} v_j(\xi_i^{exact})$ into Eq. (44), the noise value of estimated mass is expressed as:

$$m^{noise} = \frac{R_j^{noise}}{\sum_{i=1}^{nm} v_j\left(\xi_i^{exact} + \xi_i^{noise}\right)} + m^{exact} \frac{\sum_{i=1}^{nm}\left[v_j\left(\xi_i^{exact}\right) - v_j\left(\xi_i^{exact} + \xi_i^{noise}\right)\right]}{\sum_{i=1}^{nm} v_j\left(\xi_i^{exact} + \xi_i^{noise}\right)}. \tag{45}$$

It should be noted that with increasing the number of particles nm, the value m^{noise} seems in general to decrease, as predicted by Eq. (45). Numerical investigation is employed to verify this phenomenon. To simulate the Gaussian noise of frequency shifts R_j and neglecting the damping effect, the Box-Müller transformation [61] is used, which is as follows:

$$R_j^{Gauss} = \left(R_j + 1\right) \cdot \left[1 + \chi\sqrt{-2\ln u_1}\,\cos(2\pi u_2)\right] - 1, \tag{46}$$

where R_j^{Gauss} represents the frequency shift with the Gaussian noise effect; u_1 and u_2 are random numbers ranging from 0 to 1; χ is the uncertainty of the R_j^{Gauss}.

In order to investigate the influence of the uncertainty χ on the estimated results, numerical computation of the mass identification is employed, with the estimated mass $m^{estimate}$ obtained. In every uncertainty χ, 500 cases are identified with different R_j^{Gauss}, because R_j^{Gauss} is generated with the random numbers of u_1 and u_2, in Eq. (46). In every case, first six R_j^{Gauss} are used. It should be noted that the initial positions of the particles are the exact ones, to remove the influence of initial guess in the identification process. Therefore, the estimated results in these case are assumed to be

$$m^{estimate} = m^{exact} + m^{noise}. \tag{47}$$

Then, in every uncertainty χ, the relative deviations of the estimate mass, expressed as m^{noise}/m^{exact}, are used in the density estimation process [62,63], with the density results $F_\chi(m^{noise}/m^{exact})$. Consequently, The relative densities $\overline{F}_\chi(m^{noise}/m^{exact}) = F_\chi(m^{noise}/m^{exact})/F_\chi^{max}$ are plotted as the contours in Fig. 10, where F_χ^{max} is the maximum of the density F_χ in a certain uncertainty χ. In the color legend of the figure, the red color denotes the most-encountered from the samples, while the blue color denotes the least-encountered. The number and positions of particles in the Fig. 10 are: (a) one particle with position $\xi_1 = 0.2$; (b) two particles with position $\xi_1 = 0.2$ and $\xi_2 = 0.3$; (c) three particles with position $\xi_1 = 0.2$, $\xi_2 = 0.3$ and $\xi_3 = 0.4$; (d) four particles with position $\xi_1 = 0.2$, $\xi_2 = 0.3$, $\xi_3 = 0.4$ and $\xi_4 = 0.45$.

In Fig. 10, the deviation is concentrated at low uncertainty χ, while the accuracy of estimation is rapidly decreasing with the increase of uncertainty χ. When one particle participates in the identification, to obtain the estimated mass under 1% error range demands the uncertainty lower than 2×10^{-5}, with the probability more than 97.82%, which is calculated from the density curve generated from Fig. 10(a). Owing to the insensitivity of resonant frequency versus the change of attached mass, the very small changes of resonant frequencies can reflect heavy change of the attached mass in a mass identification. Therefore, to estimate the particle mass accurately needs frequency measurement in high precision. The "Allan variance" [64] is used to evaluate the measured frequencies.

From Fig. 10(a)–(d), the concentration of the deviation distribution increases with adding particles on the mass resonator. That illustrates that increasing the number of mass can improve the robustness of mass estimation, which reduces the impacts on the estimation from the noise of frequencies. Fig. 11 shows the relative density of the relative mass deviation m^{noise}/m^{exact}, at the uncertainty $\chi = 10^{-4}$. The results are read from Fig. 10, in which the peaks are sharpened and tend to $m^{noise}/m^{exact} = 0$ with particle number increasing. This phenomenon recommends multi-particles better than single particle when in mass identification, for the identification of multi-particles may improve the ability of resistance on frequency noise.

4.5. The influence of the initial guess on the position in the mass identification

The initial guess $\boldsymbol{\theta}_0$ can affect the accuracy and even correctness of the estimated mass of Eq. (37). For the nonlinear relationship between the frequency shifts R_j and particles position ξ_i, the initial positions, represented by ξ_i^0 are especially influential on the estimated results. In order to investigate the influence, we employed several numerical cases of the mass estimation results versus different initial (guessed) positions ξ_i^0, to verify the effectiveness of the estimation process, with the results shown in Fig. 12. Variable Ω is represented as the accuracy of the estimated mass, expressed as:

$$\Omega = \begin{cases} 1 - \left|\dfrac{m^{estimate} - m^{exact}}{m^{exact}}\right|, & \left|\dfrac{m^{estimate} - m^{exact}}{m^{exact}}\right| \le 1 \\ 0, & \left|\dfrac{m^{estimate} - m^{exact}}{m^{exact}}\right| > 1 \end{cases} \tag{48}$$

where $m^{estimate}$ and $|\bullet|$ denote the estimated value of mass and the absolute value, respectively. As $\Omega = 1$ represents $m^{estimate} = m^{exact}$, $\Omega = 0$ simply means an identification failure. The identification failure may be caused by an excessive error of estimation mass or the iteration failure of the iteration computation. In Fig. 12, only 2 particles are assumed to participate in the estimation, while the initial positions are $\xi_1^{exact} = 0.1$, $\xi_2^{exact} = 0.4$ in (a), $\xi_1^{exact} = 0.25$, $\xi_2^{exact} = 0.28$ in (b), $\xi_1^{exact} = 0.35$, $\xi_2^{exact} = 0.4$ in (c), $\xi_1^{exact} = 0.15$, $\xi_2^{exact} = 0.2$ in (d), $\xi_1^{exact} = 0.1$, $\xi_2^{exact} = 0.15$ in (e) and $\xi_1^{exact} = 0.45$, $\xi_2^{exact} = 0.49$ in (f) and they are marked by symbols of star. To generate these results, first six resonant frequencies are used and the step size of the initial position is 0.005.

From Fig. 12(a)–(d), a large red zone can be observed, which means that the estimation is successful. The star symbols are surrounded with the red area, which means that the initial positions close to the exact one can easily reach the success estimation. The blue zone denotes the failure estimation. However, in Fig. 12(a) and (d), the areas, whose color is not red or blue, are regarded as the pseudo success area.

There is a subtle difference between the definitions of the pseudo success and failure. The failure is defined in Eq. (48) as $\Omega = 0$. The failure estimation is easy to be distinguished, for the obvious errors can be observed, such as the estimated position out of the range of [0,1]. After applying a small shift on the initial guess, the estimated results may change significantly, which is a failure. The pseudo success is also incorrect, but is difficult to be distinguished. When the initial positions are located at the pseudo success area, the estimation result is incorrect and causes errors on the estimation. The estimated results of the pseudo success are stable after the shift on the initial guess. Therefore, it is easy to mistakenly regard the pseudo success as successful estimation. In mass identification, multiple initial guesses are necessary to identify

whether the pseudo success happens, then further verification is needed such as checking the estimated positions by SEM technology.

When the particle positions ξ_i^{exact} are closed to 0, as shown in Fig. 12 (e), due to the various errors induced by numerical algorithm, it is hard to identify the regular pattern of the results of an estimated mass. One example, which causes this error, is the boundary layer effect [65]: The similar trend of the amplitude near the fixed end of different modes, causes trouble in the fitting process. For the multiple particles identification, this effect may lead to the difficulty in the position identification. However, as shown in Fig. 12(f), the mass identification can be successful, in the conditions that the particles are near the center of beam. Different from those in Fig. 12(e) and (d), the number of resonant frequencies increases to 10, i.e., $nf = 10$. The results are shown in Fig. 13. From the figures, the problems of estimation failure and pseudo success area are not mitigated by adding the number of frequencies. Therefore, in order to maintain the effectiveness of mass estimation, it is suggested that the positions of particles should be in the range of $\xi_i^{exact} \in [0.15, 0.85]$, which can be achieved by structure design on the test system.

4.6. The simulation of the mass identification on different particle numbers

To investigate the mass sensing algorithm for different particle numbers, 100 cases of the mass identification are computed numerically for each particle number. The exact mass is set to be $m^{exact} = 0.01$, and the exact positions of the particles are generated randomly by $\xi_i^{exact} = 0.15 + 0.35\,u$, where u is a random number, ranging from 0 to 1. Thus $\xi_i^{exact} \in [0.15, 0.5]$, corresponding to the symmetrical property of the function $v_j(\xi)$. Five scenarios are tested with the particle number $nm = 1$, 2, 3, 4 and 5, respectively. The initial guess of the inversion process is fixed: Initial mass $m^0 = 0.005$; For one-particle scenario, $\xi_1^0 = 0.3$; For two-particle scenario, $\xi_1^0 = 0.25$ and $\xi_2^0 = 0.3$; For three-particle scenario, $\xi_1^0 = 0.2$, $\xi_2^0 = 0.25$ and $\xi_3^0 = 0.3$; For four-particle scenario, $\xi_1^0 = 0.2$, $\xi_2^0 = 0.25$, $\xi_3^0 = 0.3$ and $\xi_4^0 = 0.35$; For five-particle scenario, $\xi_1^0 = 0.2$, $\xi_2^0 = 0.25$, $\xi_3^0 = 0.3$, $\xi_4^0 = 0.35$ and $\xi_5^0 = 0.5$.

Fig. 14 shows the results of estimated masses in every mass sensing, at the two scenarios: 2 particles and 5 particles. The first six frequencies are used in these estimations. Most points are concentrated at the exact mass in the two scenarios. However, several points evidently deviate from the exact mass. So we introduce a result filter to block out the obvious error results, shown in the cyan area in Fig. 14. In the mass sensing, the points of $m^{\text{estimate}} > 0.011$ or $m^{\text{estimate}} < 0$ are removed.

The filtered results are processed to be the mean values and standard deviations, which are plotted in Fig. 15. When one particle is identified, the estimated mass closes to the exact one, and the standard deviation slightly deviates from zero. Clearly, the estimation results at the scenarios of $nf = 10$ are much better than those of $nf = 6$. With the increase of the particle number, the deviation of the mean masses and the standard deviations are showing an increasing trend.

5. Conclusion

The Timoshenko beam model with multiple particles is presented and approximate analytical solution for resonant frequencies is obtained. In the solution, the relationship between the resonant frequencies, the decay rate, the mass and positions of attached particles, together with the influence of viscous damping effect and axial tension, is presented. By comparing the frequency prediction results with those of FEM model and the previous studies, the present model is validated to simulate the frequency shifts lead by multiple particles adsorption. Especially, the present model more accurately describes the higher order resonant frequencies, axial stress effect, and damping effect.

To determine the mass and positions of particles, an iteration algorithm is proposed with a transformation to monotonize the relation of the indicator and position. An improved indicator of denoting the impacts of attached particles is proposed here, which is related with the shifts of frequencies and decay rates. By using the frequency shifts data of the present model and the FEM, the estimated results are close to the input data. The present mass identification process is applicable on multiple particles mass sensing, when the number of particles is less than the number of resonant frequencies. For mass identification of multiple particles, increasing the number of resonant frequencies is helpful to improve the precision.

Identifying the mass of multiple particles in every estimation process is a strategy to achieve the higher efficiency and throughput of the mass resonator system. Through the investigation on the multi-particle mass identification, the sensitivity on mass and the robustness of the mass identification are higher than those with only one particle attached. This study provides a theoretical foundation on the application of the mass identification of multi-particle mass.

CRediT authorship contribution statement

Zhang designed the research, Zhang and Wei established the model, Wei carried out the computation, Zhang and Wei wrote the paper.

Declaration of Competing Interest

The authors declare the following financial interests/personal relationships which may be considered as potential competing interests: Yin Zhang reports financial support was provided by National Natural Science Foundation of China. Yin Zhang reports financial support was provided by Chinese Academy of Sciences. Yin Zhang reports a relationship with University of the Chinese Academy of Sciences that includes: employment.

Acknowledgments

This work was supported by the National Natural Science Foundation of China (NSFC No. 11772335), the Strategic Program Research Program (B) of the Chinese Academy of Sciences (XDB22020201), the National Key Research and Development Program of China (2016YFB1200602-09 and 2016YFB1200602-10).

Appendix. A

The vibration of the undamped beam with axial tension is described by the following equation:

$$e\frac{\mathrm{d}^4\phi(\xi)}{\mathrm{d}\xi^4} - s\frac{\mathrm{d}^2\phi(\xi)}{\mathrm{d}\xi^2} - \omega^2\phi(\xi) = 0, \tag{A. 1}$$

where $e>0$, $s>0$ and the doubly clamped boundary conditions are:

$$\phi(0)=\phi(1)=\frac{\mathrm{d}\phi(0)}{\mathrm{d}\xi}=\frac{\mathrm{d}\phi(1)}{\mathrm{d}\xi}=0. \tag{A. 2}$$

The exact solution of Eq. (A. 1) is the following [66]:

$$\phi(\xi)=C^1\sin\left(g^1\xi\right)+C^2\cos\left(g^1\xi\right)+C^3\exp\left(-g^2\xi\right)+C^4\exp\left(g^2\xi\right), \tag{A. 3}$$

Here g^1 and g^2 are given as the following expressions:

$$g^1=\sqrt{\frac{\sqrt{4e\omega^2+s^2}-s}{2e}},\quad g^2=\sqrt{\frac{\sqrt{4e\omega^2+s^2}+s}{2e}}. \tag{A. 4}$$

By applying the doubly clamped boundary condition, the eigenfrequency ω can be solved by setting the following determinant zero:

$$\det[\mathbf{X}(\omega)]=0, \tag{A. 5}$$

where the matrix

$$\mathbf{X}=\begin{bmatrix} 0 & 1 & 1 & 1 \\ \sin g^1 & \cos g^1 & \exp(-g^2) & \exp(g^2) \\ g^1 & 0 & -g^2 & g^2 \\ g^1\cos g^1 & -g^1\sin g^1 & -g^2\exp\left(-g^2\right) & g^2\exp\left(g^2\right) \end{bmatrix}. \tag{A. 6}$$

Here Eq. (A.5) is a transcendental equation with infinite solutions and the solution ω_j denotes the j-th eigenfrequency. By substituting the eigenfrequency ω_j into Eq. (A. 4) and obtaining the values of g_j^1 and g_j^2, the coefficients are

$$\begin{aligned} &C_j^1=1,\quad C_j^2=\frac{g_j^1e^{g_j^2}-g_j^1e^{-g_j^2}-2g_j^2\sin\left(g_j^1\right)}{\left[2\cos\left(g_j^1\right)-e^{-g_j^2}-e^{g_j^2}\right]g_j^2},\\ &C_j^3=\frac{g_j^1\cos\left(g_j^1\right)-g_j^1e^{g_j^2}+g_j^2\sin\left(g_j^1\right)}{\left[2\cos\left(g_j^1\right)-e^{-g_j^2}-e^{g_j^2}\right]g_j^2},\quad C_j^4=\frac{g_j^1e^{-g_j^2}+g_j^2\sin\left(g_j^1\right)-g_j^1\cos\left(g_j^1\right)}{\left[2\cos\left(g_j^1\right)-e^{-g_j^2}-e^{g_j^2}\right]g_j^2}. \end{aligned} \tag{A. 7}$$

Appendix. B.

see Figs. B. 1, B. 2.

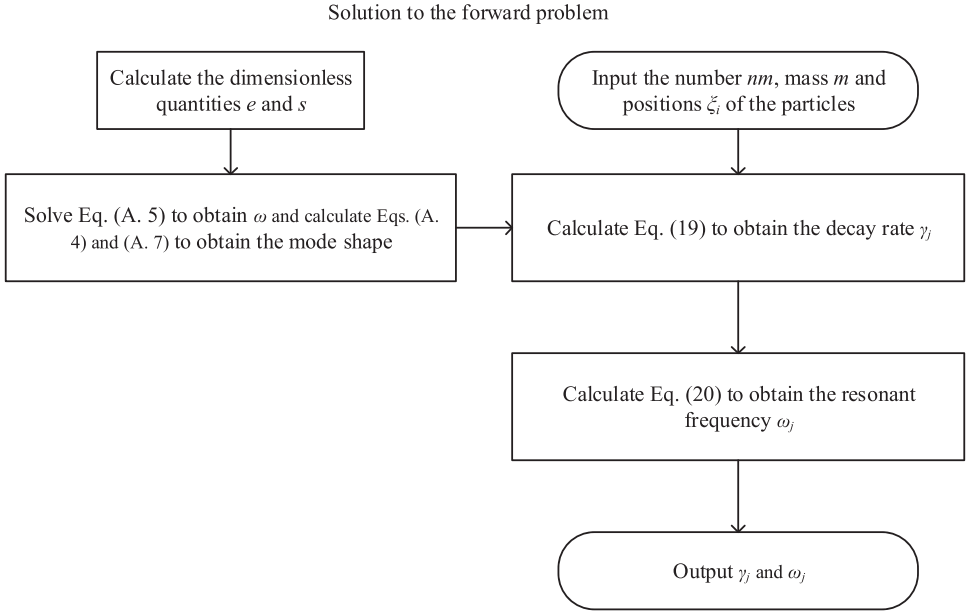

Fig. B. 1. . The flowchart of the solution to forward problem.

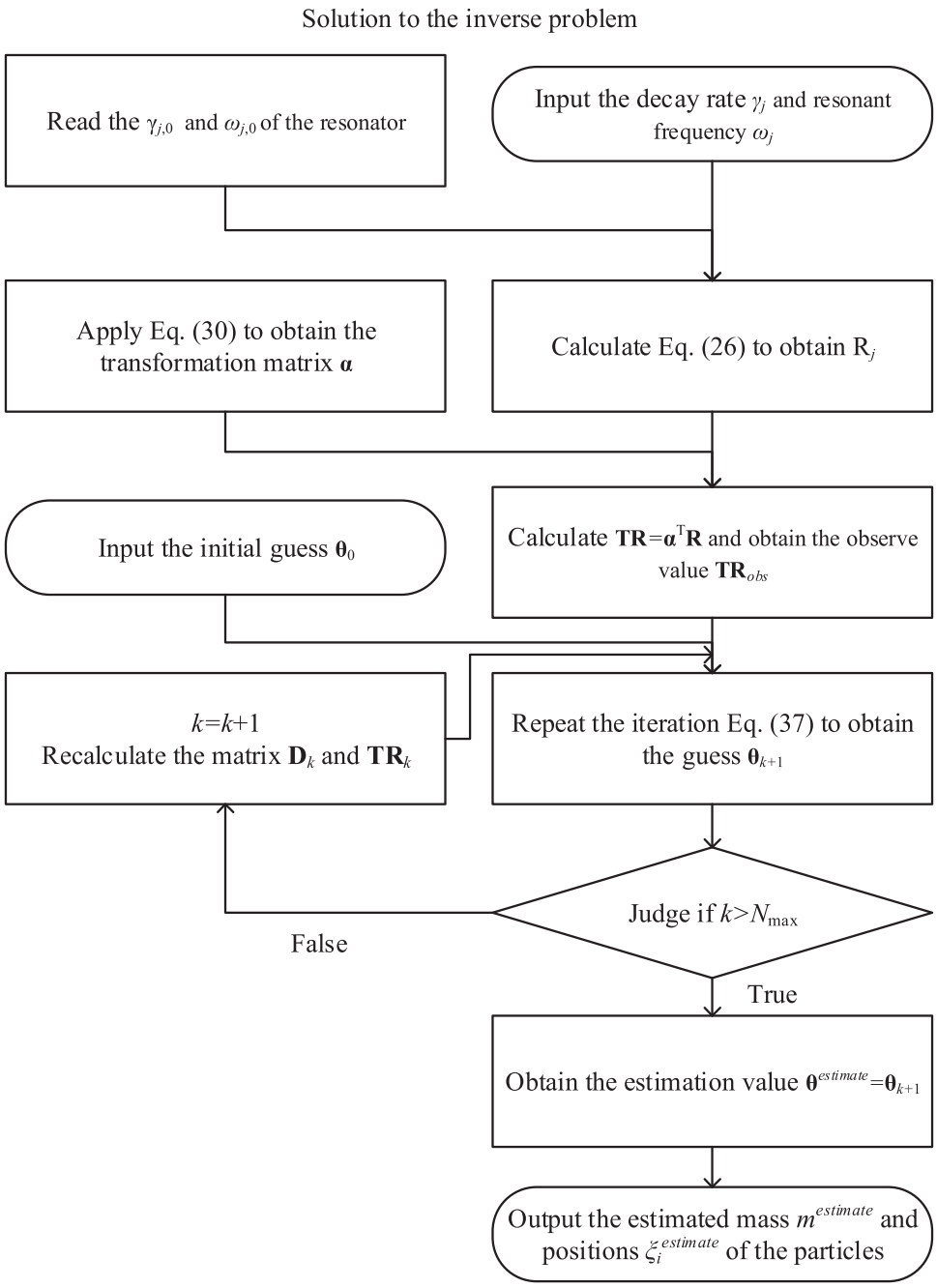

Fig. B. 2. . The flowchart of the solution to inverse problem.

References

[1] T. Braun, M.K. Ghatkesar, N. Backmann, W. Grange, P. Boulanger, L. Letellier, H. P. Lang, A. Bietsch, C. Gerber, M. Hegner, Quantitative time-resolved measurement of membrane protein–ligand interactions using microcantilever array sensors, Nat. Nanotechnol. 4 (2009) 179–185.

[2] R. Gabl, H.D. Feucht, H. Zeininger, G. Eckstein, M. Schreiter, R. Primig, D. Pitzer, W. Wersing, First results on label-free detection of DNA and protein molecules using a novel integrated sensor technology based on gravimetric detection principles, Biosens. Bioelectron. 19 (2004) 615–620.

[3] S. Dominguez-Medina, S. Fostner, M. Defoort, M. Sansa, A.K. Stark, M.A. Halim, E. Vernhes, M. Gely, G. Jourdan, T. Alava, P. Boulanger, C. Masselon, S. Hentz, Neutral mass spectrometry of virus capsids above 100 megadaltons with nanomechanical resonators, Science 362 (2018) 918–922.

[4] R. Rosario, R. Mutharasan, Piezoelectric excited millimeter sized cantilever sensors for measuring gas density changes, Sens. Actuator B Chem. 192 (2014) 99–104.

[5] J.L. Arlett, E.B. Myers, M.L. Roukes, Comparative advantages of mechanical biosensors, Nat. Nanotechnol. 6 (2011) 203–215.

[6] A. Boisen, S. Dohn, S.S. Keller, S. Schmid, M. Tenje, Cantilever-like micromechanical sensors, Rep. Prog. Phys. 74 (2011) 36101.

[7] B.N. Johnson, R. Mutharasan, Biosensing using dynamic-mode cantilever sensors: a review, Biosens. Bioelectron. 32 (2012) 1–18.

[8] J.J. Ruz, O. Malvar, E. Gil-Santos, D. Ramos, M. Calleja, J. Tamayo, A review on theory and modelling of nanomechanical sensors for biological applications, Processes 9 (2021) 164.

[9] G.Y. Chen, T. Thundat, E.A. Wachter, R.J. Warmack, Adsorption-induced surface stress and its effects on resonance frequency of microcantilevers, J. Appl. Phys. 77 (1995) 3618–3622.

[10] K. Duan, Y. Li, L. Li, Y. Hu, X. Wang, Diamond nanothread based resonators: ultrahigh sensitivity and low dissipation, Nanoscale 10 (2018) 8058–8065.

[11] M. Narducci, E. Figueras, M.J. Lopez, I. Gracia, J. Santander, P. Ivanov, L. Fonseca, C. Cané, Sensitivity improvement of a microcantilever based mass sensor, Microelectron. Eng. 86 (2009) 1187–1189.

[12] M.K. Ghatkesar, V. Barwich, T. Braun, J.P. Ramseyer, C. Gerber, M. Hegner, H. P. Lang, U. Drechsler, M. Despont, Higher modes of vibration increase mass sensitivity in nanomechanical microcantilevers, Nanotechnology 18 (2007), 445502.

[13] D. Jin, X. Li, J. Liu, G. Zuo, Y. Wang, M. Liu, H. Yu, High-mode resonant piezoresistive cantilever sensors for tens-femtogram resoluble mass sensing in air, J. Micromech. Microeng. 16 (2006) 1017.

[14] X. Le, L. Peng, J. Pang, Z. Xu, C. Gao, J. Xie, Humidity sensors based on AlN microcantilevers excited at high-order resonant modes and sensing layers of uniform graphene oxide, Sens. Actuator B Chem. 283 (2019) 198–206.
[15] F.R. Blom, S. Bouwstra, M. Elwenspoek, J.H.J. Fluitman, Dependence of the quality factor of micromachined silicon beam resonators on pressure and geometry, J. Vac. Sci. Technol. B Microelectron. Nanom. Struct. Process. Meas. Phenom. 10 (1992) 19–26.
[16] R.A. Buser, N.F. de Rooij, Very high Q-factor resonators in monocrystalline silicon, Sens. Actuator A Phys. 21 (1990) 323–327.
[17] K.L. Ekinci, Y.T. Yang, M.L. Roukes, Ultimate limits to inertial mass sensing based upon nanoelectromechanical systems, J. Appl. Phys. 95 (2004) 2682–2689.
[18] R. Sandberg, K. Mølhave, A. Boisen, W. Svendsen, Effect of gold coating on the Q-factor of a resonant cantilever, J. Micromech. Microeng. 15 (2005) 2249.
[19] L.Q. Nguyen, P.E. Larsen, S. Bishnoi, A. Boisen, S.S. Keller, Fabrication of fully suspended pyrolytic carbon string resonators for characterization of drug nano-and microparticles, Sens. Actuator A Phys. 288 (2019) 194–203.
[20] S.S. Verbridge, J.M. Parpia, R.B. Reichenbach, L.M. Bellan, H.G. Craighead, High quality factor resonance at room temperature with nanostrings under high tensile stress, J. Appl. Phys. 99 (2006), 124304.
[21] H. Li, X. Wang, H. Wang, J. Chen, The nonlocal frequency behavior of nanomechanical mass sensors based on the multi-directional vibrations of a buckled nanoribbon, Appl. Math. Model 77 (2020) 1780–1796.
[22] T.T. Yu, X.F. Zhang, Y.M. Xu, X.L. Cheng, S. Gao, H. Zhao, L.H. Huo, Low concentration H2S detection of CdO-decorated hierarchically mesoporous NiO nanofilm with wrinkle structure, Sens. Actuator B Chem. 230 (2016) 706–713.
[23] T.P. Burg, M. Godin, S.M. Knudsen, W. Shen, G. Carlson, J.S. Foster, K. Babcock, S. R. Manalis, Weighing of biomolecules, single cells and single nanoparticles in fluid, Nature 446 (2007) 1066–1069.
[24] Y. Bao, S. Cai, H. Yu, T. Xu, P. Xu, X. Li, A resonant cantilever based particle sensor with particle-size selection function, J. Micromech. Microeng. 28 (2018) 85019.
[25] A. Tarantola. Inverse Problem Theory and Methods for Model Parameter Estimation, Society for Industrial and Applied Mathematics, Philadelphia, 2005.
[26] S. Dohn, W. Svendsen, A. Boisen, O. Hansen, Mass and position determination of attached particles on cantilever based mass sensors, Rev. Sci. Instrum. 78 (2007), 103303.
[27] A. Morassi, M. Dilena, On point mass identification in rods and beams from minimal frequency measurements, Inverse Probl. Eng. 10 (2002) 183–201.
[28] A. Bouchaala, A.H. Nayfeh, N. Jaber, M.I. Younis, Mass and position determination in MEMS mass sensors: a theoretical and an experimental investigation, J. Micromech. Microeng. 26 (2016), 105009.
[29] M.S. Hanay, S. Kelber, A.K. Naik, D. Chi, S. Hentz, E.C. Bullard, E. Colinet, L. Duraffourg, M.L. Roukes, Single-protein nanomechanical mass spectrometry in real time, Nat. Nanotechnol. 7 (2012) 602.
[30] M.S. Hanay, S.I. Kelber, C.D. O'Connell, P. Mulvaney, J.E. Sader, M.L. Roukes, Inertial imaging with nanomechanical systems, Nat. Nanotechnol. 10 (2015) 339–344.
[31] Y. Zhang, Y. Liu, Detecting both the mass and position of an accreted particle by a micro/nano-mechanical resonator sensor, Sensors 14 (2014) 16296–16310.
[32] Y. Zhang, Y.P. Zhao, Mass and force sensing of an adsorbate on a beam resonator sensor, Sensors 15 (2015) 14871–14886.
[33] Y. Zhang, Y.P. Zhao, Mass and force sensing of an adsorbate on a string resonator, Sens. Actuator B Chem. 221 (2015) 305–311.
[34] A. Morassi, J. Fernández-Sáez, R. Zaera, J.A. Loya, Resonator-based detection in nanorods, Mech. Syst. Signal Process. 93 (2017) 645–660.
[35] E. Sage, M. Sansa, S. Fostner, M. Defoort, S. Hentz, Single-particle mass spectrometry with arrays of frequency-addressed nanomechanical resonators, Nat. Commun. 9 (2017).
[36] L. Zhao, F. Wang, Y.L. Zhang, X. Zhao, Theoretical study on the dynamic behavior of a plate-like micro-cantilever with multiple particles attached, PLoS One 11 (2016).
[37] S. Dohn, S. Schmid, F. Amiot, A. Boisen, Position and mass determination of multiple particles using cantilever based mass sensors, Appl. Phys. Lett. 97 (2010) 44103.
[38] A. Morassi, M. Rollo, Identification of two cracks in a simply supported beam from minimal frequency measurements, J. Vib. Control. 7 (2001) 729–739.
[39] N.T. Khiem, L.K. Toan, A novel method for crack detection in beam-like structures by measurements of natural frequencies, J. Sound Vib. 333 (2014) 4084–4103.
[40] M. Calleja, P.M. Kosaka, Á. San Paulo, J. Tamayo, Challenges for nanomechanical sensors in biological detection, Nanoscale 4 (2012) 4925–4938.
[41] M.K. Baller, H.P. Lang, J. Fritz, C. Gerber, J.K. Gimzewski, U. Drechsler, H. Rothuizen, M. Despont, P. Vettiger, F.M. Battiston, J.P. Ramseyer, P. Fornaro, E. Meyer, H.J. Güntherodt, A cantilever array-based artificial nose, Ultramicroscopy 82 (2000) 1–9.
[42] S. Cui, P. Ling, H. Zhu, H.M. Keener, Plant pest detection using an artificial nose system: a review, Sensors 18 (2018) 378.
[43] A.K. Naik, M.S. Hanay, W.K. Hiebert, X.L. Feng, M.L. Roukes, Towards single-molecule nanomechanical mass spectrometry, Nat. Nanotechnol. 4 (2009) 445–450.
[44] S. Timoshenko. Vibration Problems in Engineering, 4th ed., Wiley, New York, 1974.
[45] G.R. Cowper, The shear coefficient in timoshenko's beam theory, J. Appl. Mech. 33 (1964) 335–340.
[46] H.T. Banks, D.J. Inman, On damping mechanisms in beams, J. Appl. Mech. 58 (1991) 716–723.
[47] G.F. Wang, X.Q. Feng, Timoshenko beam model for buckling and vibration of nanowires with surface effects, J. Phys. D Appl. Phys. 42 (2009), 155411.
[48] L. Meirovitch. Fundamentals of Vibrations, McGraw-Hill, Boston, 2001.
[49] J. Tamayo, P.M. Kosaka, J.J. Ruz, Á. San Paulo, M. Calleja, Biosensors based on nanomechanical systems, Chem. Soc. Rev. 42 (2013) 1287–1311.
[50] J.E. Sader, Frequency response of cantilever beams immersed in viscous fluids with applications to the atomic force microscope, J. Appl. Phys. 84 (1998) 64–76.
[51] R.R. Grüter, Z. Khan, R. Paxman, J.W. Ndieyira, B. Dueck, B.A. Bircher, J.L. Yang, U. Drechsler, M. Despont, R.A. McKendry, B.W. Hoogenboom, Disentangling mechanical and mass effects on nanomechanical resonators, Appl. Phys. Lett. 96 (2010) 23113.
[52] C. Ma, S. Chen, F. Guo, Simultaneous determination of the mass and position of attached particles using a micro-beam resonant mass sensor with axial pre-tension, Acta Mech. 232 (2021) 4037–4055.
[53] A.P. Bovsunovsky, Efficiency of crack detection based on damping characteristics, Eng. Fract. Mech. 214 (2019) 464–473.
[54] J.J. Moré, The Levenberg-Marquardt algorithm: implementation and theory, in: Numer. Anal., Springer, Berlin, Heidelberg, 1978, pp. 105–116.
[55] M. Cui, Y. Zhao, B. Xu, X. Gao, A new approach for determining damping factors in Levenberg-Marquardt algorithm for solving an inverse heat conduction problem, Int. J. Heat Mass Transf. 107 (2017) 747–754.
[56] O. Malvar, J.J. Ruz, P.M. Kosaka, C.M. Domínguez, E. Gil-Santos, M. Calleja, J. Tamayo, Mass and stiffness spectrometry of nanoparticles and whole intact bacteria by multimode nanomechanical resonators, Nat. Commun. 7 (2016) 1–8.
[57] X. Wei, Q. Chen, S. Xu, L. Peng, J. Zuo, Beam to string transition of vibrating carbon nanotubes under axial tension, Adv. Funct. Mater. 19 (2009) 1753–1758.
[58] S. Ma, X. Wang, The impact of adsorbate mass on a nanomechanical resonator, Microsyst. Technol. 25 (2019) 3837–3846.
[59] S. Schmid, L.G. Villanueva, M.L. Roukes. Fundamentals of Nanomechanical Resonators, Springer, 2016.
[60] S. Schmid, M. Kurek, A. Boisen, Towards airborne nanoparticle mass spectrometry with nanomechanical string resonators, Micro- Nanotechnol. Sens. Syst. Appl. V 8725 (2013), 872525.
[61] G.E.P. Box, M.E. Muller, A note on the generation of random normal deviates, Ann. Math. Stat. 29 (1958) 610–611.
[62] A.W. Bowman, Applied Smoothing Techniques for Data Analysis: The Kernel Approach with S-Plus Illustrations, Clarendon Press, Oxford, 1997.
[63] B.W. Silverman. Density Estimation for Statistics and Data Analysis, Chapman and Hall, London, 1986.
[64] F.L. Walls, D.W. Allan, Measurements of frequency stability, Proc. IEEE 74 (1986) 162–168.
[65] M. Dilena, M.F. Dell'Oste, A. Morassi, R. Zaera, The role of boundary conditions in resonator-based mass identification in nanorods, Mech. Adv. Mater. Struct. (2021) 1–11.
[66] Y. Zhang, L.J. Zhuo, H.S. Zhao, Determining the effects of surface elasticity and surface stress by measuring the shifts of resonant frequencies, Proc. R Soc. A Math. Phys. Eng. Sci. 469 (2013).

Chenxi Wei, received the B.S. degree in automotive engineering from Beihang University, Beijing, China, in 2015 and the M.S. degree in solid mechanics from University of Science and Technology Beijing, Beijing, China, in 2019. He is currently working toward the Ph.D. degree in solid mechanics, in the State Key Laboratory of Nonlinear Mechanics (LNM), Institute of Mechanics, Chinese Academy of Sciences (CAS). His current research focuses on the dynamics and the inverse problems in the sensors applications.

Yin Zhang, BS, Department of Mechanics, Peking University, Beijing, China, 1997 and Ph. D., Department of Mechanical Engineering, University of Connecticut, Storrs, Connecticut, USA, 2003. From 2003 to 2004, he worked as an assistant professor in the State Key Laboratory of Nonlinear Mechanics (LNM), Institute of Mechanics, Chinese Academy of Sciences (CAS) and as an associate professor from 2004 to 2012, and since 2012, as a professor. His current research focuses on the MEMS/NEMS structural mechanics, dynamics and the inverse problems in the sensors applications.